NASA/TM—2014–21857

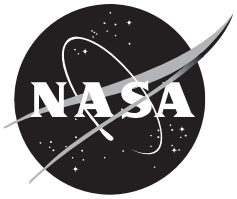

High Resolution Mapping of Soils and Landforms for the Desert Renewable Energy Conservation Plan (DRECP)

Christopher S. Potter
NASA Ames Research Center, Moffett Field, California

Shuang Li
California State University Monterey Bay, Seaside, California

January 2014

NASA STI Program

Since its founding, NASA has been dedicated to the advancement of aeronautics and space science. The NASA scientific and technical information (STI) program plays a key part in helping NASA maintain this important role.

The NASA STI program operates under the auspices of the Agency Chief Information Officer. It collects, organizes, provides for archiving, and disseminates NASA's STI. The NASA STI program provides access to the NTRS Registered and its public interface, the NASA Technical Reports Server, thus providing one of the largest collections of aeronautical and space science STI in the world. Results are published in both non-NASA channels and by NASA in the NASA STI Report Series, which includes the following report types:

- TECHNICAL PUBLICATION. Reports of completed research or a major significant phase of research that present the results of NASA Programs and include extensive data or theoretical analysis. Includes compilations of significant scientific and technical data and information deemed to be of continuing reference value. NASA counter-part of peer-reviewed formal professional papers but has less stringent limitations on manuscript length and extent of graphic presentations.

- TECHNICAL MEMORANDUM. Scientific and technical findings that are preliminary or of specialized interest, e.g., quick release reports, working papers, and bibliographies that contain minimal annotation. Does not contain extensive analysis.

- CONTRACTOR REPORT. Scientific and technical findings by NASA-sponsored contractors and grantees.

- CONFERENCE PUBLICATION. Collected papers from scientific and technical conferences, symposia, seminars, or other meetings sponsored or co-sponsored by NASA.

- SPECIAL PUBLICATION. Scientific, technical, or historical information from NASA programs, projects, and missions, often concerned with subjects having substantial public interest.

- TECHNICAL TRANSLATION. English-language translations of foreign scientific and technical material pertinent to NASA's mission.

Specialized services also include organizing and publishing research results, distributing specialized research announcements and feeds, providing information desk and personal search support, and enabling data exchange services.

For more information about the NASA STI program, see the following:

- Access the NASA STI program home page at http://www.sti.nasa.gov

- E-mail your question to help@sti.nasa.gov

- Phone the NASA STI Information Desk at 757-864-9658

- Write to:
  NASA STI Information Desk
  Mail Stop 148
  NASA Langley Research Center
  Hampton, VA 23681-2199

NASA/TM—2014–218357

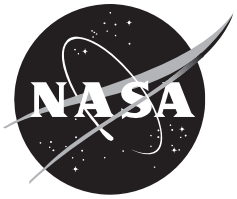

High Resolution Mapping of Soils and Landforms for the Desert Renewable Energy Conservation Plan (DRECP)

Christopher S. Potter
NASA Ames Research Center, Moffett Field, California

Shuang Li
California State University Monterey Bay, Seaside, California

Prepared for
The Renewable Energy Action Team
U.S. Bureau of Land Management California Office

National Aeronautics and
Space Administration

Ames Research Center
Moffett Field, California

January 2014

Acknowledgments

The authors thank James Weigand, Tom Pogacnik, and Matthew Bobo of the U. S. Bureau of Land Management for technical guidance and support in the analysis of satellite imagery to monitor renewable energy development zones.

Available from:

NASA Center for AeroSpace Information
7115 Standard Drive
Hanover, MD 21076-1320
443-757-5802

Acronyms Used

IDL	Interactive Data Language
DEM	Digital Elevation Model
NED	National Elevation Dataset
NASA	National Aeronautics and Space Administration
NASA JPL	NASA Jet Propulsion Laboratory
ASF	Alaska Satellite Facility
Landsat 5 TM	Landsat 5 Thematic Mapper
NAIP	National Agriculture Imagery Program
DOQQs	Digital Ortho Quarter Quad Tiles
ALOS/PARSAR	Advanced Land Observing Satellite / Phased Array L-band Synthetic Aperture Radar
NLCD	National Land Cover Database
TIGER	Topologically Integrated Geographic Encoding and Referencing
SAR	Synthetic Aperture Radar
USGS	United States Geological Survey
USDA	United States Department of Agriculture
DN	the quantized and calibrated Digital Numbers for each cell of satellite image
FLAASH	Fast Line-of-sight Atmospheric Analysis of Spectral Hypercubes
CCM	Compressed County Mosaics
NDVI	Normalized Difference Vegetation Index
NIR band	Near-infrared band
R band	Red band
HH polarization	Horizontal Transmit - Horizontal Receive Polarization
HV polarization	Horizontal Transmit - Vertical Receive Polarization
BSCI	Biological Soil Crusts Index
BTLS	Bi-temporal layer stack
RGBC	Red Green Blue Clustering
COSICorr	Co-registration of Optically Satellite Imagery and Correlation

Glossary of Terms

Interferometry	A set of techniques that superimposes waves, usually electromagnetic waves, to extract information about the waves to measure small displacements, refractive index changes and surface irregularities
Landsat Level 1T	Standard Terrain Correction - provides systematic radiometric and geometric accuracy by incorporating ground control points while employing a DEM for topographic accuracy. Geodetic accuracy of the product depends on the accuracy of the ground control points and the resolution of the DEM used: Ground control points used for Level 1T correction come from the GLS2000 data set. DEM sources include SRTM, NED, CDED, DTED, and GTOPO 30.
Reflectance	The fraction of incident electromagnetic power that is reflected at an interface, in contrast to the reflection coefficient, which is the ratio of the reflected to incident electric field.
Atmospheric Corrections	The process of removing the effects of the atmosphere on the reflectance values of images taken by satellite or airborne sensors.
HH polarization	A mode of radar polarization where the microwaves of the electric field are oriented in the horizontal plane for both signal transmission and reception by means of a radar antenna.
HV polarization	A mode of radar polarization where the microwaves of the electric field are oriented in the horizontal plane for signal transmission, and where the vertically polarized electric field of the backscattered energy is received by the radar antenna.
Terrain Correction	The process to remove the geometric distortions from a radar image due to terrain relief.
Incidence Angle	The angle defined by the incident radar beam and the vertical (normal) to the intercepting surface.
Histogram matching	A method in image processing of color adjustment of two images using the data histograms.

List of software tools used in this report

- Python 2.7 (Python Software Foundation, Download here)
- ArcGIS 10.1 (Environmental Systems Research Institute, Inc.)
- ENVI 5.0 (Exelis Visual Information Solutions, Inc.)
- ASF MapReady 3.1.22 (Alaska Satellite Facility, Download here)
- PolSARpro 4.2.0 (European Space Agency, Download here)
- Spectroradiometer data processing (GER 1500, Spectra Vista Corporation)

List of remote sensing images used in this report

- DEM 10 m (from USGS)
- Landsat 5 TM (from USGS)
- NAIP DOQQs imagery (from USDA)
- ALOS/PALSAR (from Alaska Satellite Facility)

List of auxiliary data

- National Land Cover Database 2006 (NLCD2006, Download here)
- Federal and State managed lands in California (Modified: 01/03/2014, Download here)
- TIGER/Line® All Roads County based Shapefile (2013, Download here)
- TIGER/Line® Linear Hydrography County based Shapefile (2013, Download here)

All the Python/ArcPy scripts have been developed using Python 2.7, which couples to the spatial analysis model of ArcGIS 10/10.1. An IDL package from the NASA Jet Propulsion Laboratory has been used to investigate sand dune migration in Palen Dune area. This IDL package was developed for image analysis with the ENVI 4.x platform, but it works as well under the latest ENVI 5.x version.

High Resolution Mapping of Soils and Landforms for the Desert Renewable Energy Conservation Plan (DRECP)

Introduction

The Bureau of Land Management (BLM) is playing a key role in achieving national goals of generating more electricity from renewable energy sources. The BLM allows access to federal lands for renewable energy development, helping California and the rest of the country reach a secure and reliable energy future. The Desert Renewable Energy Conservation Plan (DRECP), a major component of California's renewable energy planning efforts, is intended to provide effective protection and conservation of desert ecosystems, while allowing for the sensible development of renewable energy projects.

The DRECP was prepared through a collaborative effort between the California Energy Commission, California Department of Fish and Game, the BLM, and the U.S. Fish and Wildlife Service, also known as the Renewable Energy Action Team. The DRECP will result in efficient biological mitigation and conservation, providing renewable project developers with permit timing and cost certainty under the federal and California Endangered Species Acts, while at the same time preserving, restoring and enhancing natural communities. Approximately 22.5 million acres (9.1 million hectares) of federal and non-federal southern California desert land are within the DRECP area.

The California BLM is in the process of defining program plans for results-based adaptive biological mitigation and conservation related to renewable energy projects. From these program plans, developers of renewable projects will be provided greater certainty about required permits and permitting processes, time schedules in the planning and implementation phases, and costs for environmental compliance with the Federal and California Endangered Species Acts. Regulatory agencies and the general public will have greater assurance that natural communities and associated ecosystem functions will be preserved, restored, and enhanced for future generations.

This NASA mapping report was developed to support the DRECP. We outline in this document remote sensing image processing methods to deliver new maps of biological soils crusts, sand dune movements, desert pavements, and sub-surface water sources across the DRECP area. We focused data processing first on the largely unmapped areas most likely to be used for energy developments, such as those within Renewable Energy Study Areas (RESA) and Solar Energy Zones (SEZs). We used imagery (multispectral and radar) mainly from the years 2009-2011.

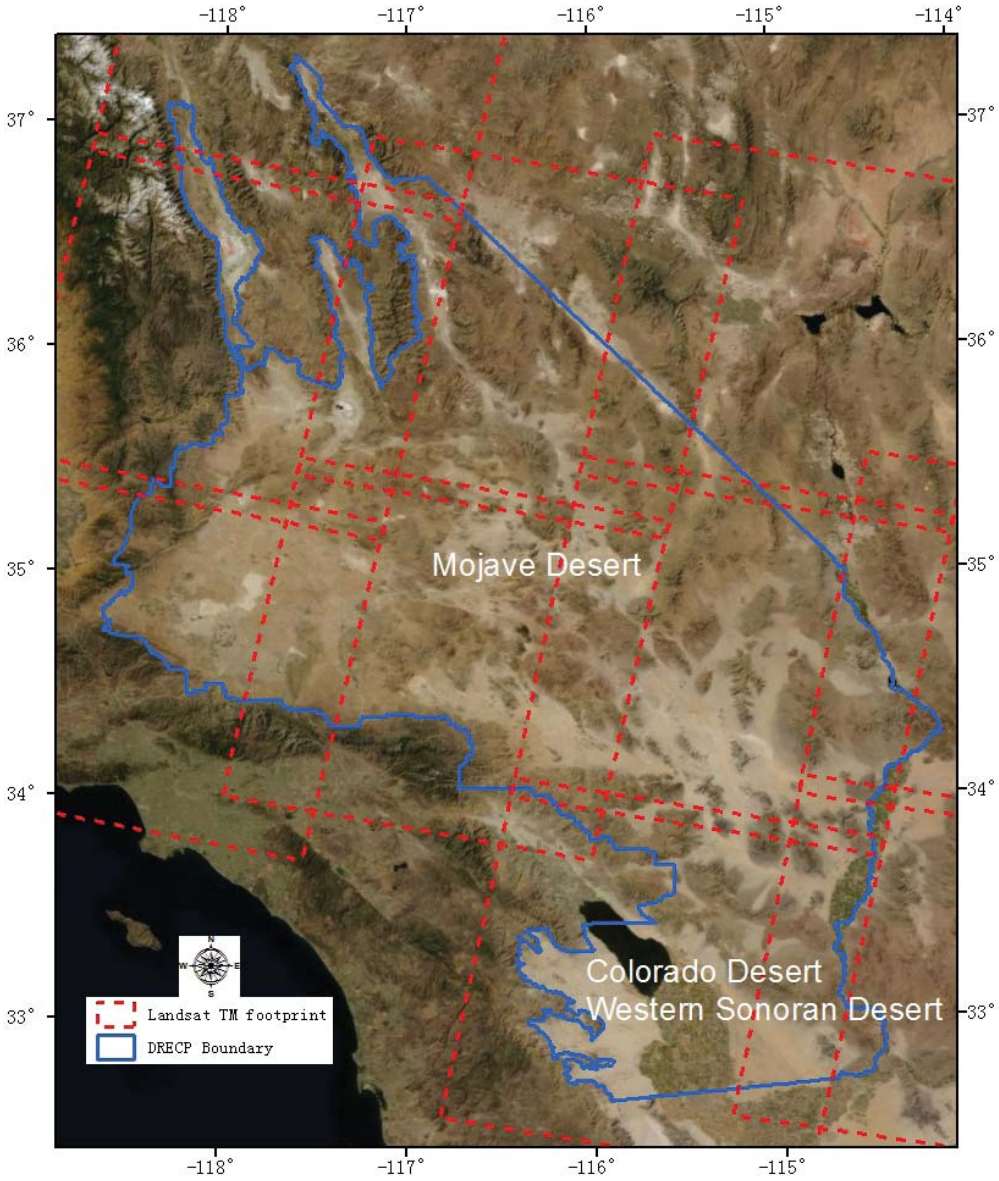

Figure 1.-- Area of desert features mapping with remote sensing. The DRECP boundary line is shown in blue and the outlines of available Landsat TM scenes is shown in dashed red lines.

The geographic focus area for the DRECP includes parts of the Great Basin, Mojave, and western Sonoran (or Colorado) Deserts, as well as ecotones of these desert communities with the adjacent ecosystems in the Sierra Nevada, Tehachapi Mountains, Transverse Ranges (Western Transverse Ranges, San Gabriel, and San Bernardino mountains), and Peninsular Ranges (Baldwin et al., 2002; DRECP, 2010) (Figure 1).

The geographic scope for this NASA mapping work was eastern Riverside County from Hayfield Dry Lake area east to the Colorado River with proposed renewable energy development areas, and Desert Conservation Lands under consideration as part of the DRECP. The mapping area totals to approximately 2.9 million acres (1.2 million hectares), or 12% of the total DRECP area (Figure 2).

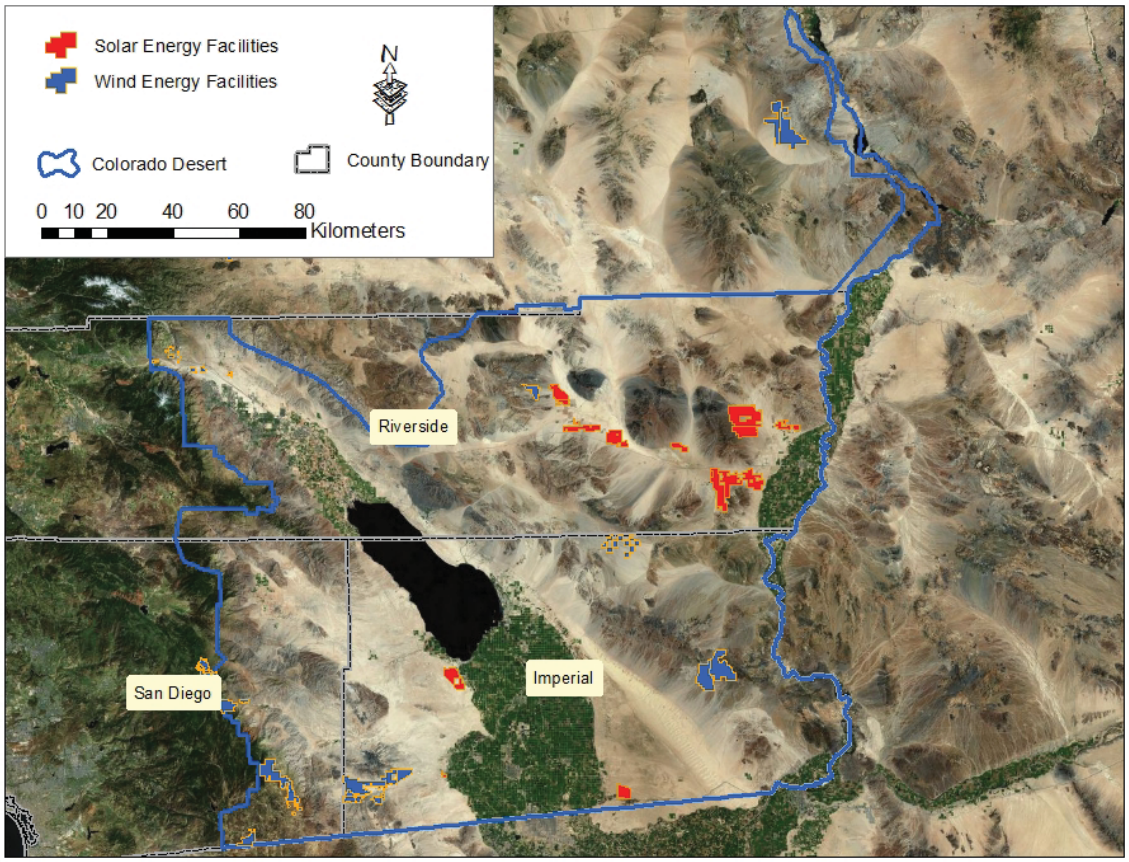

Figure 2.-- Landsat5 TM Mosaic Images of Colorado Desert. A true color image using TM bands 3(Red), 2(Green), and 1 (blue) (Images captured in Aug. 2011)

Data Preparation for Desert Mapping

Digital Elevation Models (DEM data)

DEM data at 10-m spatial resolution were acquired from the National Elevation Dataset (NED) 1/3-arc-second dataset. NED is the primary elevation data product of the USGS (http://ned.usgs.gov). Slope (gradient, or rate of maximum change in z-value) from each cell of the DEM raster surface was calculated using the Spatial Analysis Model of ArcGIS 10.1 (Figure 3). Only the regions with lower terrain fluctuation are considered possible locations to develop renewable energy facilities. We detected slopes less than 13 degrees as the natural break point to delineate these primary mapping areas (Figure 4).

For each cell in the DEM layer, the ArcGIS slope tool calculates the maximum rate of change in value from that cell to its neighbors. Eight neighbor cells are used to determine the maximum change in elevation over a specified distance. The equation below shows how the rates of change (delta) of the surface in the horizontal (dz/dx) and vertical (dz/dy) directions from the center determine the slope.

$$slope_{degrees} = ATAN\left(\sqrt{\left[\frac{dz}{dx}\right]^2 + \left[\frac{dz}{dy}\right]^2}\right) * 57.29578 \quad (1)$$

The value 57.29578 shown here is the truncated value of 180/π.

The slope layer was further processed to mask out all the cells with slopes greater than 13 degrees and exclude them from further analysis (Figure 3).

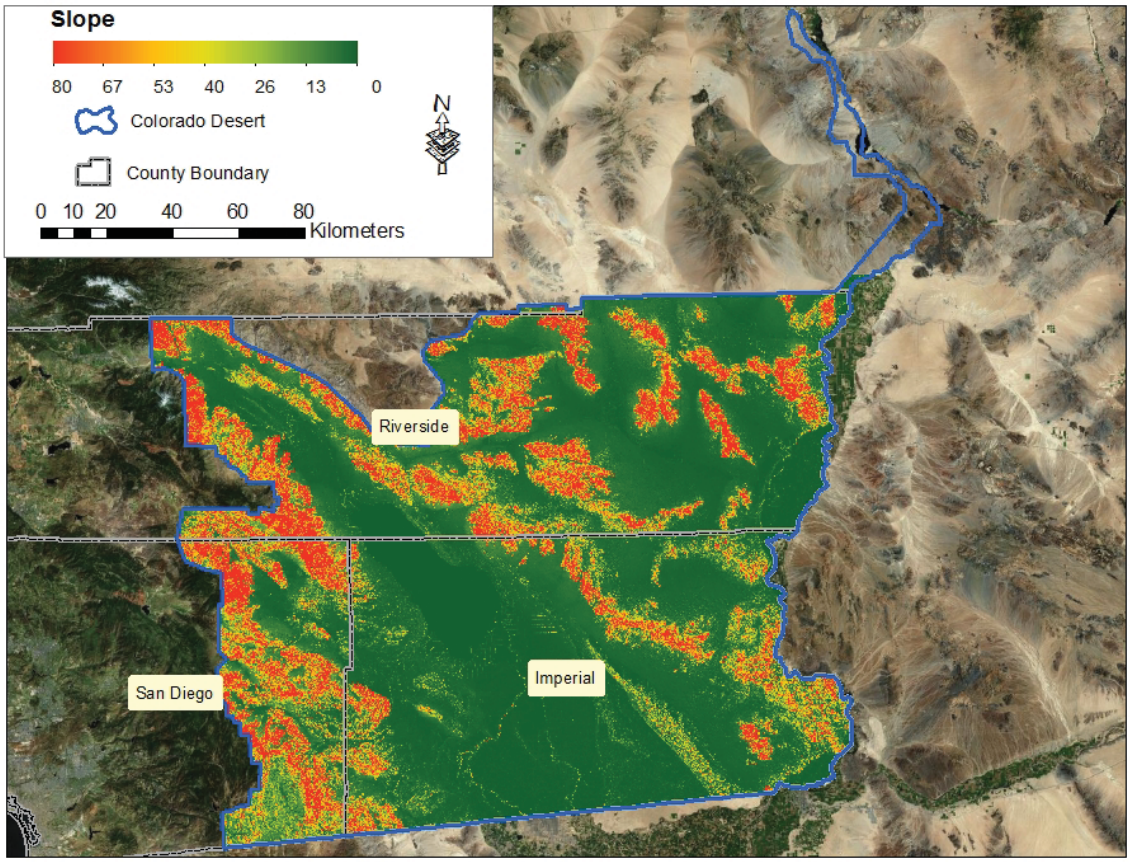

Figure 3.-- Slope Distribution across Colorado Desert

Our rationale for this slope threshold selection of 13 degrees was as follows:

- According to the Executive Summary of the Solar Energy PEIS for BLM lands, "Applications may include some lands with up to 10% slope where higher slopes inclusions meet all of the following: (1) are proximate to variance lands in the application, (2) are not otherwise excluded from development, (3) allow for the avoidance or minimization of resource conflicts, and (4) do not create any significant new or additional conflicts. In such cases, a land use plan amendment would have to be adopted as part of the project-specific analysis to permit the slope exception." See: http://solareis.anl.gov/documents/fpeis/Solar_FPEIS_ExecutiveSummary.pdf
- According to information in Table 4.1 – Summary of Key Solar Energy Technology Attributes in Solar Energy Development on DoD Installations in the Mojave and Colorado Deserts (January 2012)
- Anticipating that the technology for solar panels will advance quickly, so that a slightly broader range of undulating terrains will be suitable for use.

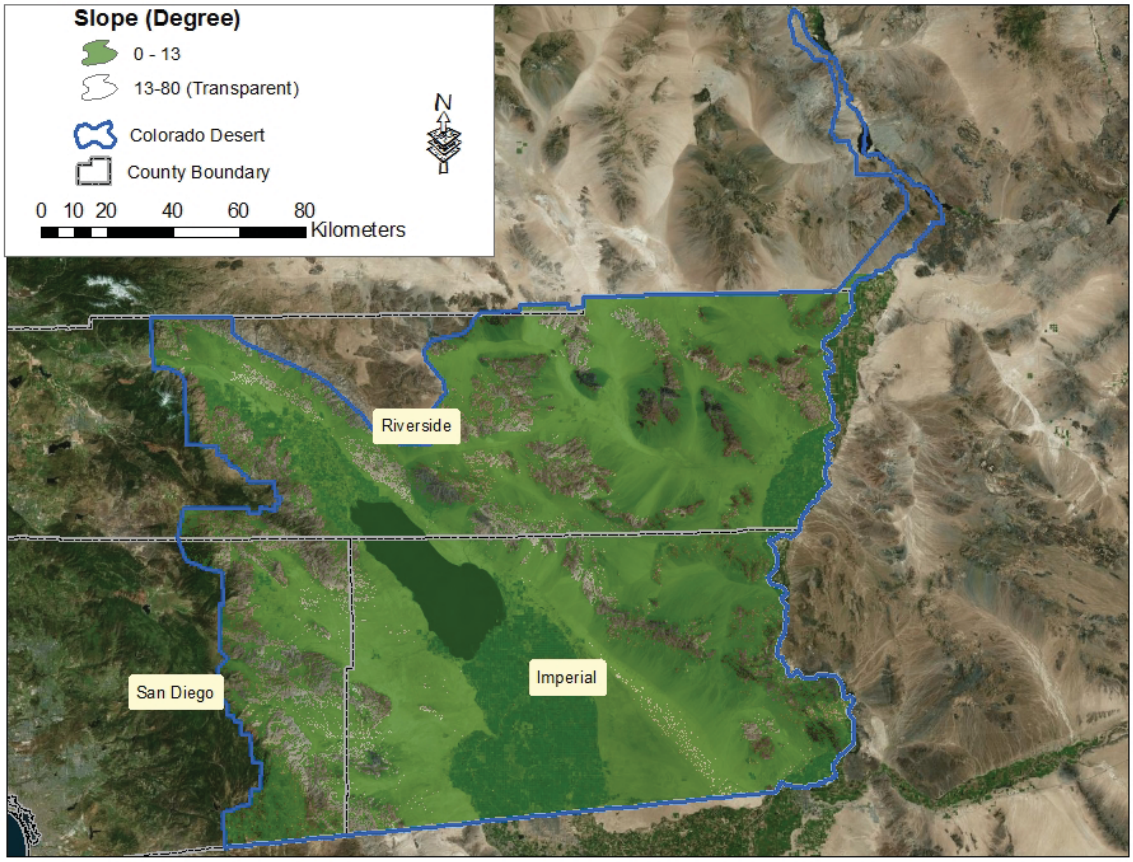

Figure 4.-- Study areas with slope less than 13 degrees

The study area was then further divided into sub-sections referred to in this study within Common Resource Area (CRA) maps (Figure 5).

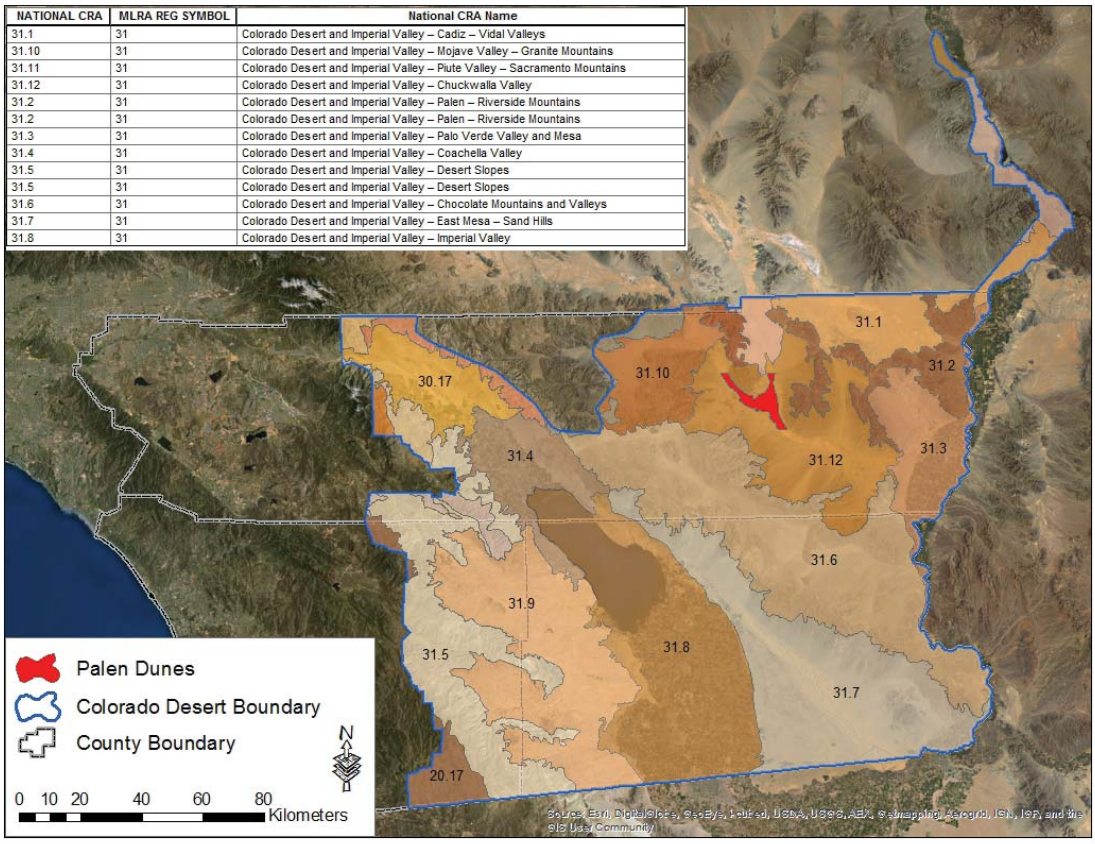

Figure 5.-- National Coordinated Common Resource Area geographic database for the DRECP area

Landsat TM images

The Landsat program has been providing uninterrupted imagery of Earth since 1972. Landsat 5 Thematic Mapper (TM) images were used in this project for mapping biological soil crust, desert pavements and varnishes, and active sand dune movements. The Landsat 5 TM image sets for the study area included path/row 038/036, 039/036, 040/036, 038/037, 039/037, and 040/037 (Figure 6). Images were selected according to the degree of atmospheric interference (primarily due to clouds). The sun elevation and sun azimuth were also considered as important factors for Landsat image selection (rationale are stated below).

Vegetation cover, soil crusts, dune texture, morphological parameters and dune mineralogical composition are critical factors for desert mapping (Mohamed and Verstraeten, 2012). Studies have shown that when the sun direction is perpendicular to a dune crest or at the stoss side and the sun elevation angle is greater than 30 degrees, the shading effect with regard to the dune profile is pronounced. Variations of sun elevation and sun azimuth of Landsat TM scenes were plotted in Figure 6. For southern California, it was concluded that the best time window for sand dune detection would be July and August.

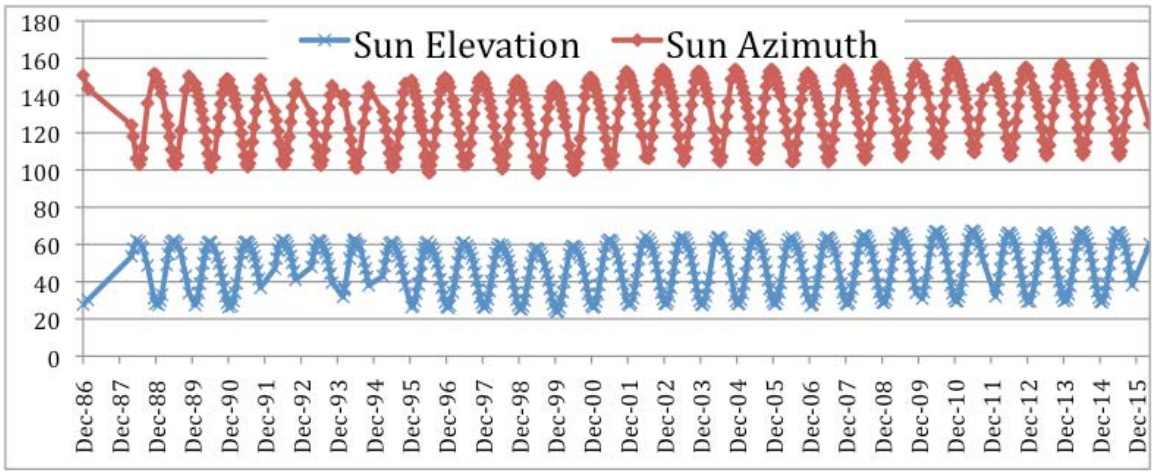

Figure 6.-- The sun elevation and sun azimuth of Landsat TM5 scenes (southern California coverage)

As an example, Landsat images covering Palen Dunes were listed in Table 1. Sun azimuth in the area ranged from 116˚to 136˚, which is nearly perpendicular to the crest orientation of the dunes. Thus, important morphological features of the dunes may be identifiable using the spectral properties of the Landsat TM images.

Table 1.-- Landsat 5 TM images for mapping of sand dune migration

Acquisition Date	Image ID	Sun Azimuth	Sun Elevation
2000-09-16	LT50390372000260XXX02	136.69	50.88
2001-08-02	LT50390372001214LGS01	114.80	60.38
2002-08-21	LT50390372002233LGS01	122.13	56.24
2003-08-08	LT50390372003220PAC04	116.35	58.96
2004-08-26	LT50390372004239PAC01	127.90	56.73
2005-08-13	LT50390372005225PAC01	122.49	60.04
2006-08-16	LT50390372006228PAC01	125.84	60.52
2007-08-19	LT50390372007231PAC01	127.26	59.97
2008-08-05	LT50390372008218PAC01	118.12	61.01
2009-08-08	LT50390372009220PAC01	120.46	61.16
2010-08-11	LT50390372010223EDC00	122.19	60.88
2011-08-14	LT50390372011226PAC01	123.08	60.13

Landsat 5 TM scenes from the USGS EarthExplorer (http://earthexplorer.usgs.gov/) archive were processed with Standard Terrain Correction (Level 1T). Level 1T provides systematic radiometric and geometric accuracy by incorporating ground control points while employing a DEM for topographic accuracy.

Image calibration, atmospheric correction, and scene mosaicing were applied to these Landsat scenes before further image transformation and analysis were conducted (Figure 7). We developed Interactive Data Language (IDL) scripts to process these Landsat scenes automatically. For calibration, we converted the 8-bit satellite-quantized digital numbers (DNs) into top-of-atmosphere (TOA) spectral reflectance using the radiometric gain and offset values associated with the Landsat TM image. For atmospheric correction, a Fast Line-of-sight Atmospheric Analysis of Spectral Hypercubes (FLAASH) module based on MODTRAN4 in the ENVI software package was applied (Adler-Golden et al., 1999). Atmospheric correction requirements were minimal for these Landsat scenes (Song et al., 2001), since aerosol contamination was extremely limited across south California desert in the summer months.

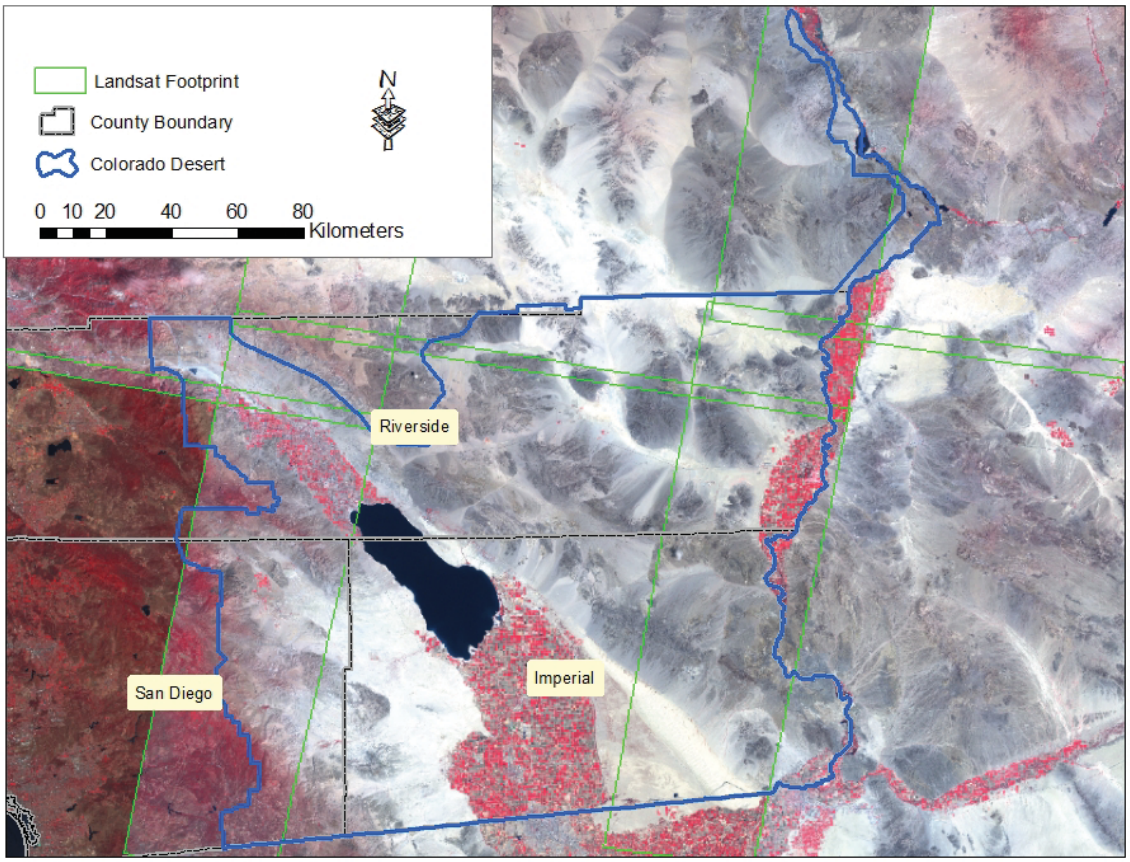

Figure 7.-- The coverage of Landsat TM5 footprints for the study area (Images captured in Aug. 2011).

- Calibration

Calibration attempts to compensate for radiometric errors from sensor defects, variations in scan angle, and system noise, resulted in images that represented true spectral radiance. ENVI 5.0 reads parameters (e.g., gains, offsets, solar irradiance, sun elevation, and acquisition time) from the Landsat MTL file (Level-1 metadata). Reflectance was computed using the following equation:

$$\rho_\lambda = \frac{\pi L_\lambda d^2}{ESUN_\lambda sin\theta} \qquad (2)$$

Where:

$$L_\lambda = Radiance\ in\ units\ of \frac{W}{m^2 * sr * um}$$

?? $L_\lambda = Radiance\ in\ units\ of \frac{W}{m^2 * sr * um}$ $L_\lambda = Radiance\ in\ units\ of \frac{W}{m^2 * sr * um}$

$L_\lambda = Radiance\ in\ units\ of \frac{W}{m^2 * sr * um}$ $L_\lambda = Radiance\ in\ units\ of \frac{W}{m^2 * sr * um}$

$$L_\lambda = Radiance\ in\ units\ of \frac{W}{m^2 * sr * um}$$

(e.g. watts per square meter per steradian when *λ* the wavelength is given in *um*)
d = Earth to sun distance, in astronomical unit (au, 1 *au is equal to* 149.6*106 *km, or* 2.956*106 *mi)*
*ESUNλ = Solar irradiance in units of W/(m2*um)*
θ = Sun elevation in degrees

- Atmospheric Corrections

Atmospheric corrections included adjustments to account for Rayleigh scattering, gaseous absorption, and aerosol scattering in three visible channels (480 nm, 560 nm, and 660 nm), and the near-infrared (NIR) channel (830 nm). Atmospheric constituents such as water vapor and ozone are extracted from climatology data sets, while aerosol optical depths (AODs) are derived from the Landsat 5 TM scene itself by adopting the dark target approach.

The current FLAASH version includes the following features:

1) Correction for the adjacency effect (pixel mixing due to scattering of surface-reflected radiance)
2) An option to compute a scene-average visibility (aerosol/haze amount) for handling the presence of clouds and stress-inducing atmospheric conditions, such as cirrus and opaque cloud classification map, and adjustable spectral polishing for artifact suppression.

FLAASH starts from a standard equation for spectral radiance at a sensor pixel, L, that applies to the solar wavelength range (thermal emission is neglected) and flat, Lambertian materials or their equivalents. The equation applied was as follows:

$$L = \left(\frac{A\rho}{1 - \rho_e S}\right) + \left(\frac{B\rho_e}{1 - \rho_e S}\right) + L_a \qquad (3)$$

Where:
ρ = the pixel surface reflectance
ρ_e = an average surface reflectance for the pixel and a surrounding region
S = the spherical albedo of the atmosphere
L_a = the radiance back scattered by the atmosphere
A and B are coefficients that depend on atmospheric and geometric conditions, but not on surface conditions.

NAIP Imagery

The National Agriculture Imagery Program (NAIP) acquires aerial imagery during the agricultural growing seasons for the continental U.S. We collected three year (2005, 2009, and 2010) of NAIP image data in Compressed County Mosaics (CCMs). CCMs are available for free download through the USDA Geospatial Data Gateway, http://datagateway.nrcs.usda.gov/ and provide high resolution (1-meter) seamless coverage images in Red, Green and Blue (or RGB) bands.

We also ordered 2009 and 2012 NAIP digital ortho quarter quad tiles (DOQQs) across the study area. Each individual image tile covered a 3.75 x 3.75 minute quarter quadrangle plus a 300-meter buffer on all four sides with 1-m resolution and 4 bands (RGB and Near Infrared). More than 2200 DOQQs image tiles in Geotiff were ordered from USDA - Aerial Photography Field Office (Figure 8) for the study area. The NAIP images were used in addition to Landsat imagery for mapping biological soil crusts and sand dune delineation.

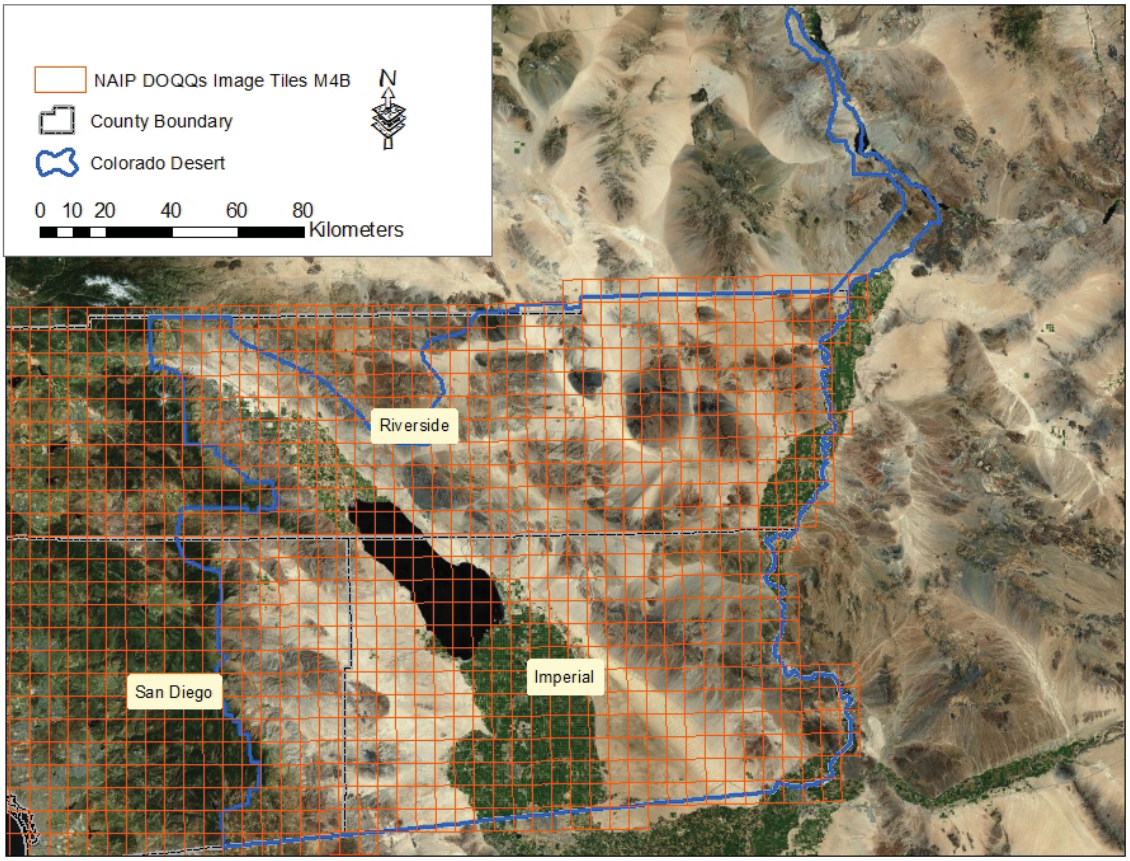

Figure 8.-- The coverage of NAIP DOQQs image tiles

The Normalized Difference Vegetation Index (NDVI) used to map relative density of green vegetation cover. NDVI takes advantage of the contrast of the characteristics of two bands from multispectral remote sensing images: the chlorophyll pigment absorption in the red band and the high reflectivity of plant materials in the NIR band.

The documented and default NDVI equation is:

$$NDVI = \frac{NIR - R}{NIR + R} \quad (4)$$

where *NIR* are pixel reflectance values from the near-infrared band and *R* values are the pixel reflectance values from the red band.

The raster layer of NDVI had values between -1.0 and 1.0. In this study, any negative values are mainly generated from water, and values near zero are mainly generated from rock outcrops, sand sheets, and desert pavements. Moderate NDVI values (0.2 to 0.3) corresponded to desert shrub and grassland or cropland.

To render the NDVI layer in ArcGIS with a specific color ramp, the equation used was as follows:

$$NDVI = \frac{NIR - R}{NIR + R} * 100 + 100 \qquad (5)$$

$$NDVI = \frac{NIR - R}{NIR + R} * 100 + 100 \qquad (5)$$

$$NDVI = \frac{NIR - R}{NIR + R} * 100 + 100 \qquad (5)$$

A NDVI layer was created from NAIP imagery as an auxiliary mask map of 1-m resolution green vegetation cover (Figure 9).

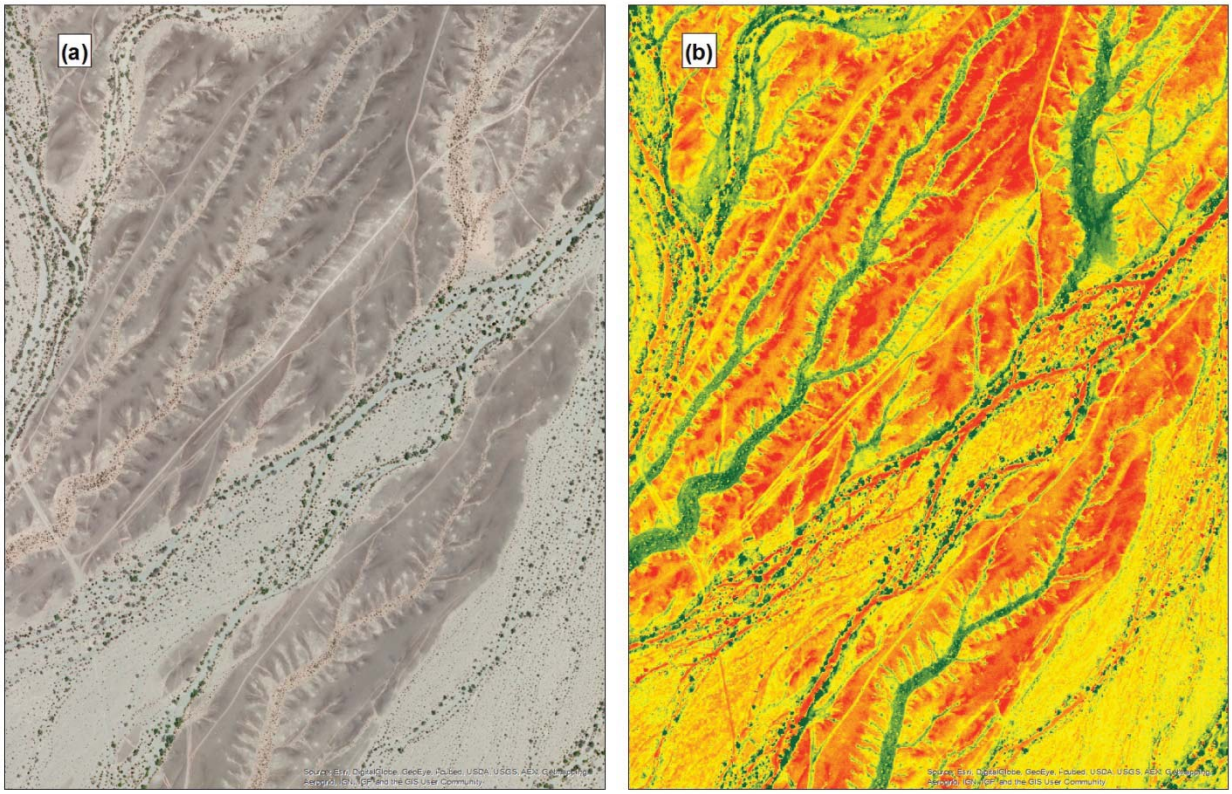

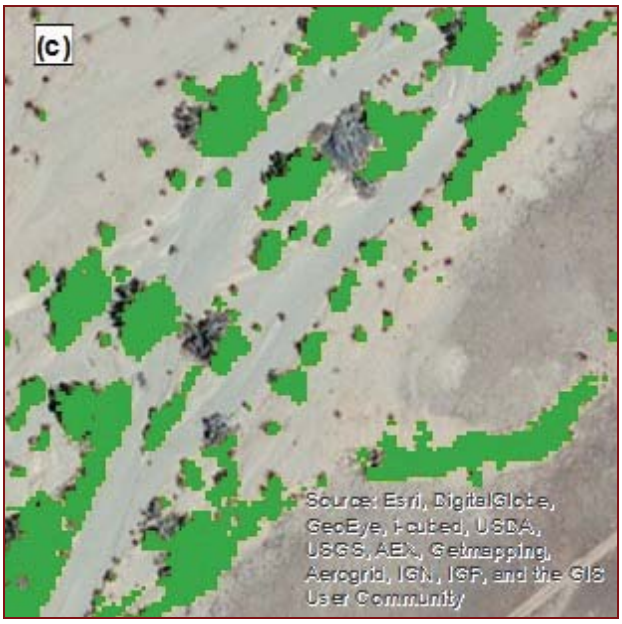

Figure 9.-- NAIP NDVI layers. (a)True color image, (b) NDVI layer, (c) Vegetation mask layer derived from NDVI.

Radar (ALOS/PALSAR) data

Spaceborne L-band SAR data from the ALOS/PALSAR sensor was acquired for the study area. We collected PALSAR data sets at 2008-4-14 with Fine Beam Single polarization (FBS, look angle 34.3˚, HH-polarization, and a 6.25m×6.25m ground resolution) and 2008-7-18 with Fine Beam Double Polarization (FBD, look angle 34.3˚, HH- and HV-polarization, ground resolution approximately 12.5m×12.5m). In FBS mode, ALOS/PALSAR can be operated with either HH- or VV-polarization with a bandwidth of 28 MHz. In FBD mode, the polarization options are HH/HV or VV/VH (HH/VV not possible) at 14-MHz bandwidth. FBS polarization (HH or VV) and FBD polarization (HH+HV or VV+VH) of PALSAR data have a varied look angle between 7° and 51° (8-60° incidence angle). The operating sensor frequency is 1.27GHZ, which corresponds to a wavelength of 23.6 cm (L-band). The Alaska Satellite Facility (ASF) provides range compression using Fast Fourier Transform (FFT), secondary range compression using range migration compensation, range migration curvature corrections, azimuth compression, multi-look processing and performed conversion from slant to ground range (PALSAR User's Guide, 1st edition, March 2006).

In order to eliminate the influence of (sub)surface soil moisture on radar signals, annual average temperature and precipitation records from the Thermal and Blythe weather stations were used to delimit the selection window of PALSAR images (Figure 10 & Figure 11, http://www.geog.ucsb.edu/~joel/g148_f09/, last accessed Feb 20, 2013). The average minimum precipitation time period across the study region was from April to June. Average temperature peaks appeared in July. PALSAR images captured within this time window (Apr - Jul) were collected for potential subsurface landform analysis (Figure 12).

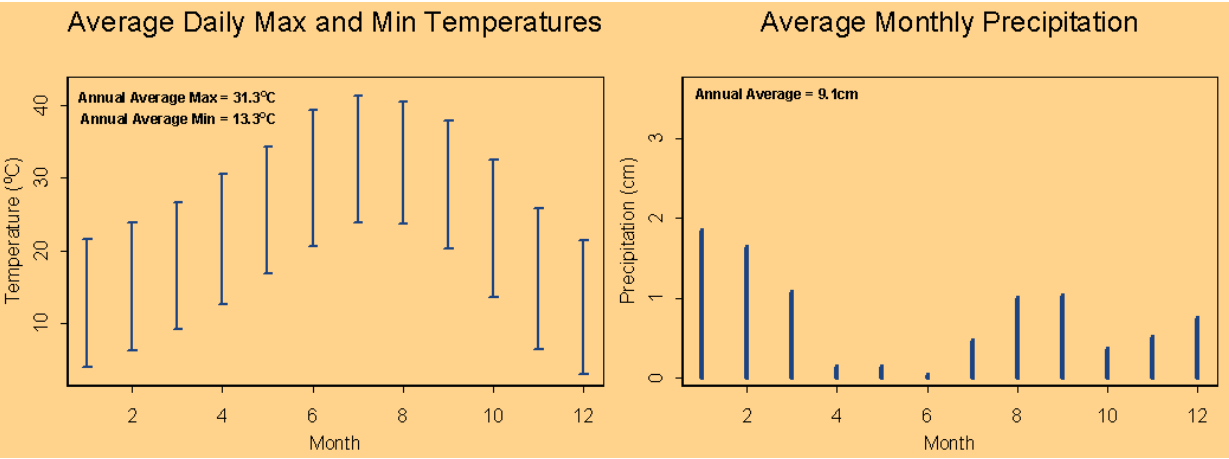

Figure 10.-- Thermal Temperature and Precipitation Salton Trough - Elevation = -34m

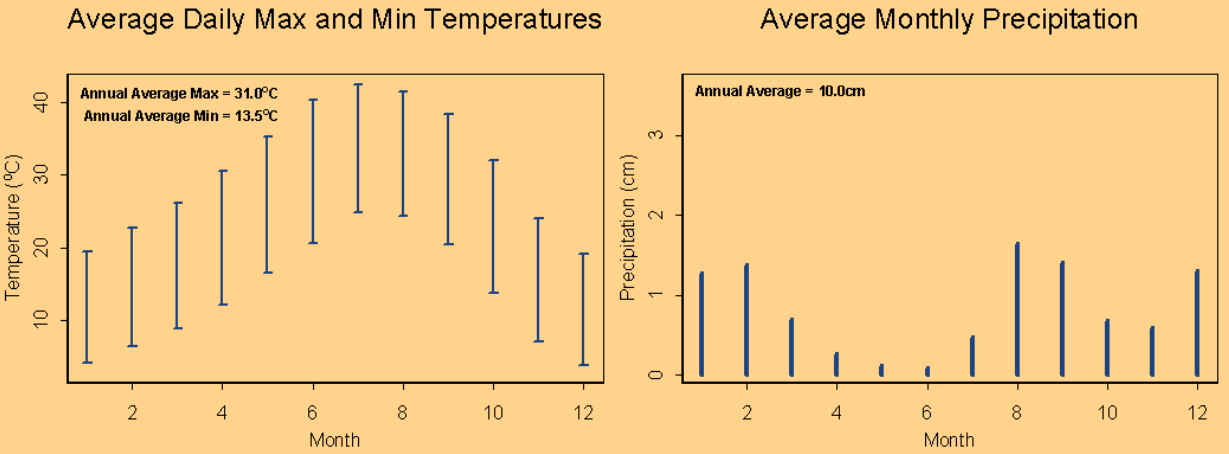

Figure 11.-- Blythe Temperature and Precipitation - Elevation = 82m

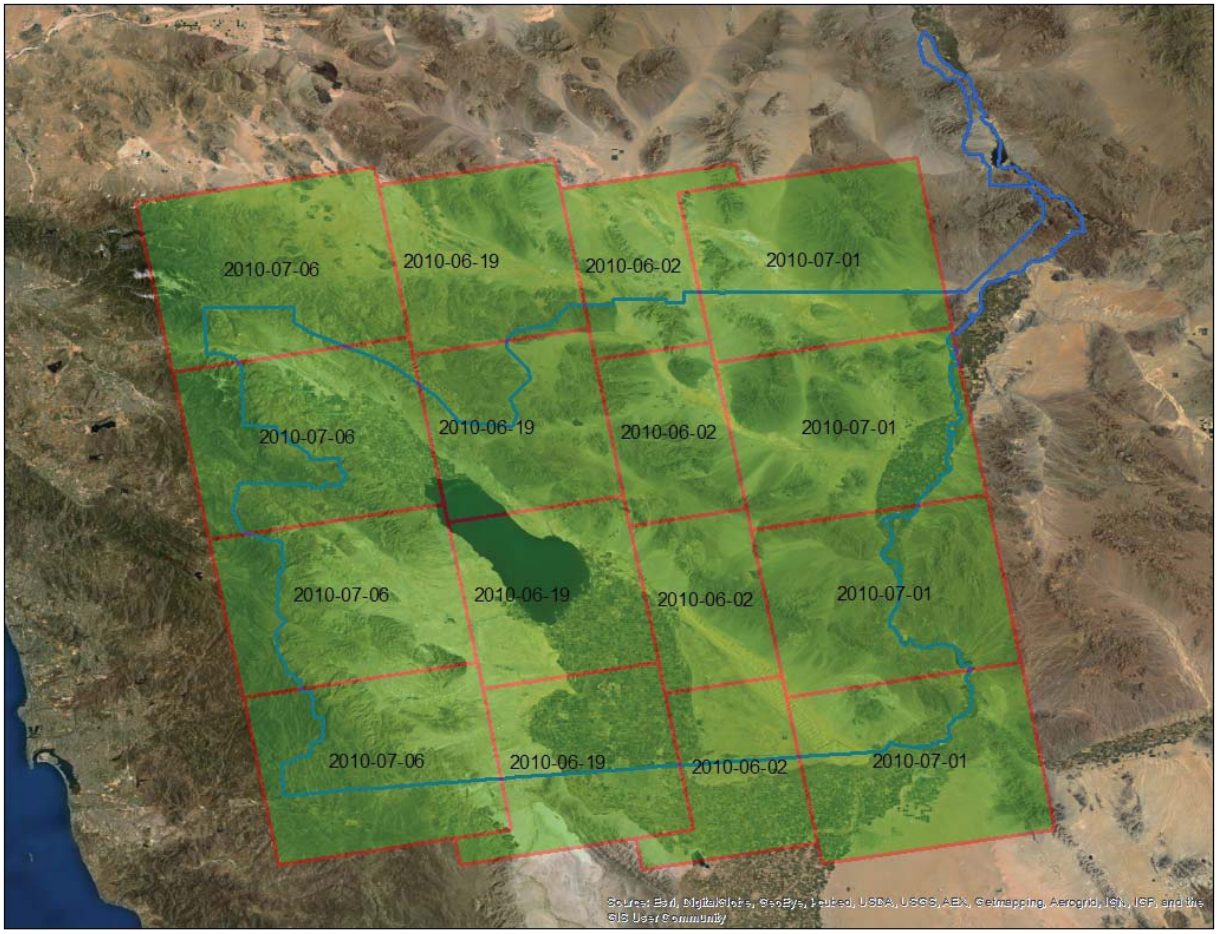

Figure 12.-- Footprint of PALSAR scenes in FBD mode

L-band images from PALSAR were acquired for June/July 2010 (12.5m, HH and HV polarization) coinciding with dry season, and for November/December 2010 (12.5m, HH and HV polarization) coinciding with wet season (**Table 2**).

Table 2. -- Listing of PALSAR imagery datasets collected.

ID	Name	Observation Mode	Polarization	Capture Date
1	ALPSRP231960640	FBD	HH/HV	2010-06-02
2	ALPSRP231960650	FBD	HH/HV	2010-06-02
3	ALPSRP231960660	FBD	HH/HV	2010-06-02
4	ALPSRP231960670	FBD	HH/HV	2010-06-02
5	ALPSRP234440640	FBD	HH/HV	2010-06-19
6	ALPSRP234440650	FBD	HH/HV	2010-06-19
7	ALPSRP234440660	FBD	HH/HV	2010-06-19
8	ALPSRP234440670	FBD	HH/HV	2010-06-19
9	ALPSRP236190640	FBD	HH/HV	2010-07-01
10	ALPSRP236190650	FBD	HH/HV	2010-07-01
11	ALPSRP236190660	FBD	HH/HV	2010-07-01
12	ALPSRP236190670	FBD	HH/HV	2010-07-01
13	ALPSRP236920640	FBD	HH/HV	2010-07-06
14	ALPSRP236920650	FBD	HH/HV	2010-07-06
15	ALPSRP236920660	FBD	HH/HV	2010-07-06
16	ALPSRP236920670	FBD	HH/HV	2010-07-06
17	ALPSRP254570640	FBD	HH/HV	2010-11-04
18	ALPSRP254570650	FBD	HH/HV	2010-11-04
19	ALPSRP254570660	FBD	HH/HV	2010-11-04
20	ALPSRP254570670	FBD	HH/HV	2010-11-04
21	ALPSRP257050640	FBD	HH/HV	2010-11-21
22	ALPSRP257050650	FBD	HH/HV	2010-11-21
23	ALPSRP257050660	FBD	HH/HV	2010-11-21
24	ALPSRP257050670	FBD	HH/HV	2010-11-21
25	ALPSRP258800640	FBD	HH/HV	2010-12-03
26	ALPSRP258800650	FBD	HH/HV	2010-12-03
27	ALPSRP258800660	FBD	HH/HV	2010-12-03
28	ALPSRP258800670	FBD	HH/HV	2010-12-03

SAR image processing steps

MapReady software version 3.1.22 (http://www.asf.alaska.edu/downloads/software_tools), developed by ASF, has been used to process ALOS/PALSAR imagery.

- Step 1: Radiometric calibration

Calibrating a SAR image involves the process of converting a linear amplitude image into a radiometrically calibrated power image. The input image is in units of digital numbers (DNs), where the output image is in units of β°, γ°, or σ°. Backscatter is the portion of the outgoing radar signal that the target redirects directly back towards the radar antenna. It is a measure of the reflective strength of a radar target (**Figure 13**). The normalized measure of the radar return

from a distributed target is called the backscatter coefficient, σ˚ or sigma naught, and is defined per unit area on the ground. If the signal formed by backscatter is undesired, it is called clutter. Other portions of incident radar energy may be reflected and scattered away from the radar or absorbed. The radar backscatter coefficient σ˚ is the ratio of the power that comes back from a patch of ground to the power sent to the patch of ground, and serves as a quantitative reference measure to the ground.

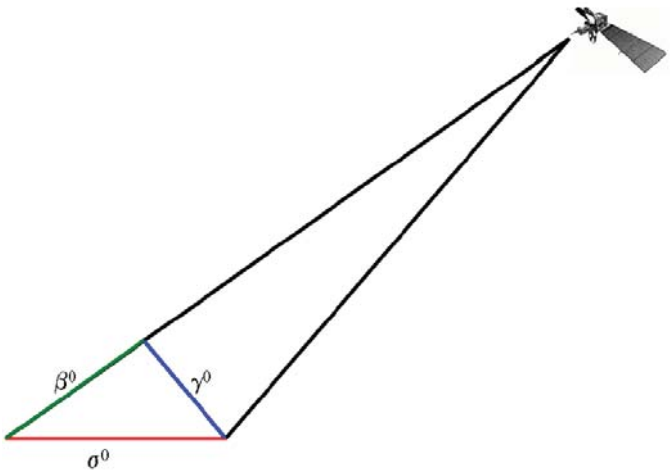

Figure 13.-- Geometric properties of radar signal

σ˚ can be retrieved from SAR images by using the following equation:

$$\sigma^0 = a_2(DN^2 - a_1 N_r) \qquad (6)$$

$$??\sigma^0 = a_2(DN^2 - a_1 N_r) \qquad (6)$$

where DN = the digital number of the original pixel value
Nr = the noise offset as a function of range
a_1 = the noise scale factor determined during processor calibration
a_2 = a linear conversion factor determined during processor calibration.

The σ˚ value resulting from the equation above is in a power scale. Converting these values into decibel (dB) values uses the following relationship:

$$dB = 10 * log_{10}(power\ scale) \qquad (7)$$

- Step 2: Terrain Correction

SAR images are acquired with side-looking geometry. This format leads to a number of distortions in the imagery: foreshortening, layover, and shadow (**Figure 14**). Terrain correction removes these geometry-induced distortions by using a DEM. The process of terrain correction includes geometric terrain correction and radiometric terrain correction. Geometric terrain correction adjusts the individual pixels of an amplitude image to be in their proper locations. Radiometric terrain correction adjusts the brightness of the pixels with respect to the

observation geometry, defined by the incidence angle as well as the slope and aspect of the local terrain.

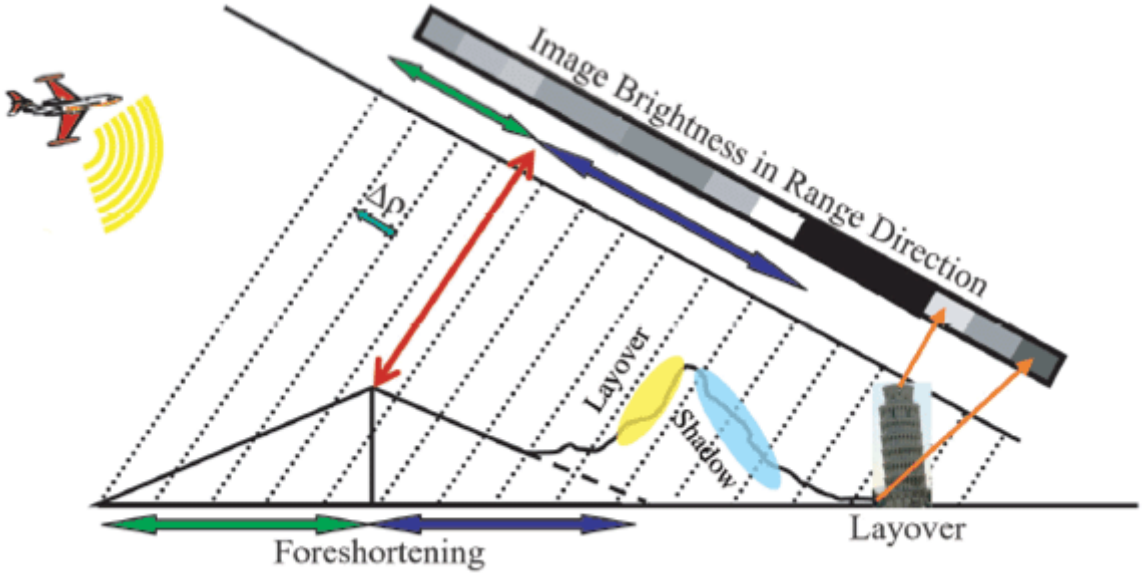

Figure 14.-- Schematic of how terrain can appear to lean left towards the satellite path with foreshortening, layover, and shadow effects

- Step 3: Geocoding

The geocoding step is essential to correlate the SAR image geometry to the real world. By transforming the image from SAR geometry into one of the standard map projections, the SAR image can be imported into ArcGIS or ENVI for further analysis. The geocoding step is invoked by turning on the “Geocode” module from MapReady. A UTM projection was used in this study. For the PALSAR scene of the I-10 corridor, the parameters for UTM zone 11N and the WGS84 datum have been used. As part of the transformation from SAR geometry into map-projected space, a bilinear method resampled the data through interpolation. Compared to nearest-neighbor and bicubic approaches, the bilinear interpolation scheme considers four neighboring pixel values and typically leads to satisfactory results.

- Step 4: Speckle filtering

SAR images were filtered to reduce the effect of speckle by utilizing a Kuan filter with a 3×3 kernel in ENVI 5.0. The resultant imagery preserved the mean values, while decreasing the standard deviation of homogeneous targets, and visually preserving the feature edges.

Desert Mapping Methodologies

Ben-Dor el al (2009) presented an overview of the case studies that have used remote sensing technologies for desert mapping applications. After a review of more than 100 literature citations pertinent to the spectral characteristics of desert soils, we selected those methodologies most readily applicable to the DRECP areas in southern California. The algorithms adopted from these peer-reviewed methodologies have largely been field-validated for acceptable accuracy in the published studies cited below.

Biological soil crusts

Biological Soil Crusts (BSCs) consist of cyanobacteria, algae, microfungi, lichens and bryophytes in varying proportions, living within or immediately on top of the uppermost millimeters of soil. Over the past two decades, a number of research studies have been conducted to investigate the spectral characteristics of BSCs or its species components (Chen et al., 2005). Graetz and Gentle (1982) examined the relationship between reflectance in the Landsat wavebands and the composition of semi-arid shrub rangeland in Australia. Ager and Milton (1987) investigated the spectral reflectance of lichens and their effects on the reflectance of rock substrates. Jacobberger (1989) focused on the reflectance characteristics and surface processes in stabilized dune environments. Karnieli and his collaborators (Karnieli & Tsoar, 1995; Pinker & Karnieli, 1995; Karnieli et al., 1996; Tsoar & Karnieli, 1996; Karnieli & Sarafis, 1996; Karnieli et al., 1997; Karnieli et al., 1999; Karnieli et al., 2001) published a series of papers to explore the relationship between spectral characteristics and the structure and function of soil crusts in semi-arid and arid environments.

The most popular vegetation index, the Normalized Difference Vegetation Index (NDVI), has been applied to capture the properties of BSCs during wet periods (Burgheimer et al., 2006; Karnieli et al., 1999). The Crust Index (CI) proposed by Karnieli et al. (1997, 1999) took advantage of the unique spectral phenomenon of BSCs. Not unlike NDVI, the CI was based on the normalized difference between the red and the blue spectral bands:

$$\mathrm{CI} = 1 - \frac{(\mathrm{R_{red}} - \mathrm{R_{blue}})}{(\mathrm{R_{red}} + \mathrm{R_{blue}})} \qquad (8)$$

Chen et al. (2005) developed an improved Biological Soil Crust Index (BSCI) to map soil crusts in desert area:

$$\mathrm{BSCI} = \frac{1 - L \times |R_{red} - R_{green}|}{R_{GRNIR}^{mean}} \qquad (9)$$

The BSCI can be treated as an enhancement of spectral features of the biological crusts in green, red and NIR bands of Landsat TM images. It yields higher values for the presence BSCs, relative to the background of bare sand and dry plant material. We therefore selected the BSCI to map the BSC distribution across the study area of southern California. Compared to the CI, BSCI does not include a blue band, but is sensitive to lichen-dominated BSCs. The higher the lichen percent coverage, the higher the BSCI value would be expected. The parameter value of

L and the threshold of BSCI (Equation 9 above) may be refined in the future, based on additional field-based spectral measurements of BSCs.

Desert varnish and pavements

Desert varnish is a hard, dark-brown or black coat, dull or lustrous (if wind polished) that accumulates on the exposed surfaces of rock fragments and outcrops. Its composition is independent of the composition of the host rock (Potter and Rossman, 1979). A desert pavement is a desert surface that is covered with closely packed, interlocking angular or rounded rock fragments of pebble and cobble size (Cooke and Warren, 1973; see Summary of Varnish and Summary of Desert Pavement).

Beratan and Anderson (1998) developed an approach to map alluvial geomorphic surfaces in California. Visible bands and the NIR band of Landsat TM images were used to compose a newly developed spectral space, which provided information about the composition and topography of desert surfaces. This spectral space can readily be classified as young, intermediate, or old in terms of stages of development. This approach was successfully applied to mapping in the southern Whipple Mountains portion of the Mojave Desert. We applied the methods of Beratan and Anderson (1998) in this study. The image processing flowchart and definitions of surface classifications were provided in

Figure **15** and Table 3.

Table 3.-- Association of spectral categories with geomorphic surfaces definitions (after Beratan and Anderson, 1998)

Image class	Stage	Description
S1	1	Currently active drainage system. Pronounced bar-and-swale morphology. Sand, with scattered larger clasts. Minimal vegetation, concentrated along channel margins.
S2	1	Abandoned drainages that have not been inactive long enough for soils, rock varnish or pavements to develop. Similar to S1, but with somewhat larger clasts. Vegetation along the margins.
S3	½	Clasts dominate over sand, but clast-to-clast contacts are rare. Bar-and-swale morphology less pronounced than in S1, S2. Rock varnish present as thin, discontinuous veneer. A small amount of scattered vegetation.
S4	2	Well-developed rock varnish, pavements. Bar-and-swale morphology almost entirely subdued. Covered by interlocking mosaics of clasts. Some small cacti in spaces between clasts.
S5	2	Similar to S4, but disrupted by gullies, with well-developed desert pavement preserved only on the ridges between gullies.
S6	3	More heavily dissected than S5, with little preserved pavement. Clast mosaic disrupted, leaving a veneer of thickly varnished clasts. Scattered fragments of caliche.
S7	3	Highly dissected, with no intact pavemented surface remaining. Typically sloping, forming banks of gullies and small washes.

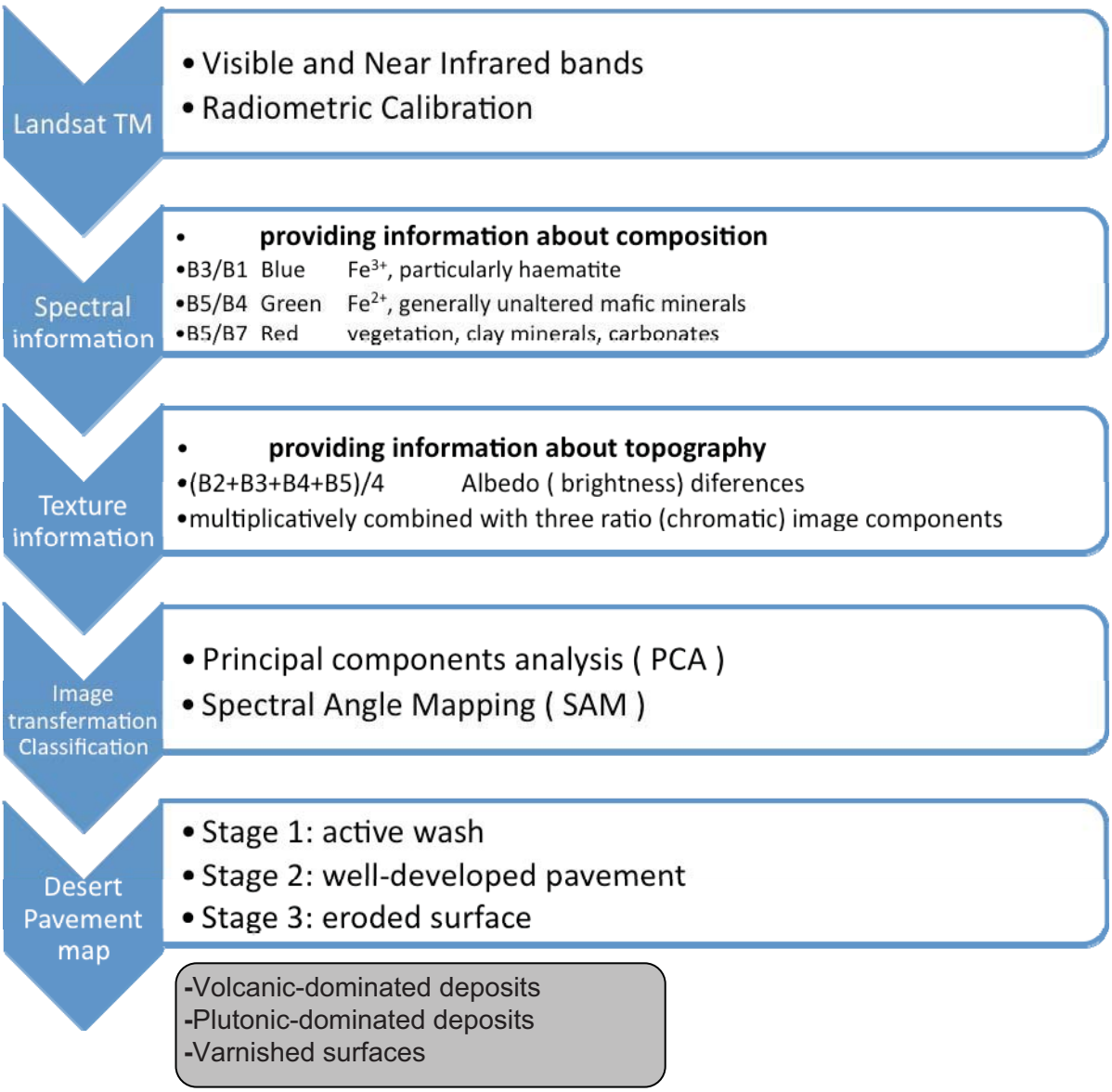

Figure 15.-- Image processing flowchart of desert pavements using the four-component technique

Sand dune movements

Through the 1980s and 1990s, studies of the geomorphology of desert sand dunes were dominated by field studies of wind flow and sand flow over individual dunes (Livingstone et al., 2007). However, field-based approaches can rarely cover large areas of dune movements. Modeling methods have been shown to complement field-based approaches (Mohamed and Verstraeten, 2012). The combined use of remote sensing imagery, long-term GPS measurements, and GIS has enabled the mapping of large dune area movements.

The research of Livingstone et al. (2007) and Mohamed and Verstraeten (2012) provided comprehensive reviews of recent progress in studies of desert dune movements (Table 4). The U.S. Geological Survey (USGS) scientists successfully conducted remote sensing research for monitoring of sand dune movement in the Sonoran Desert (Redsteer et al., 2011). The

comparison of GPS mapping results from these previous USGS studies in Arizona showed that optical remote sensing could provide a high level of accuracy for sand dune monitoring (see Appendix 1 of this report). Two latest published algorithms (from Mohamed and Verstraeten, 2012; Hermas, et al., 2012) were selected for application to sand dune migration monitoring in this study.

Table 4.-- Approaches used in geomorphological studies of desert sand dunes (Livingstone et al., 2007)

Field survey	Attempts to measure the stresses imposed by the wind on the sand surface proved challenging, and the use of shear (or friction) velocity as a surrogate for shear stress also failed to deliver effective results.	
Modeling approaches	Considering desert sand dunes as complex system, Werner (1995) modeled the development of dune field patterns. Kocurek and Ewing (2005) described non-linear modeling to examine sand dunes as self-organized complex systems. Hardware in wind tunnels was used in the modeling approaches.	
Remote sensing	Aerial photography	Historical records
	Optical imagery	Advanced Very High Resolution Radiometer (AVHRR), Landsat TM imagery, ASTER, SPOT, Quickbird (Mohamed and Verstraeten, 2012)
	Radar detection	Spaceborne Imaging Radar (SIR-C), Radarsat, and LIDAR images

- Bi-Temporal Layer Stacking (BTLS) for multi-temporal Landsat TM images

We have acquired 10 cloud free scenes each year over the Mojave Desert region and southern California for sand dune mapping. The RGB and NIR bands of TM images was used to determine the extent to which sand dunes have shifted over the past 20 years. This mapping can provide a baseline for years before and after the development of renewable energy infrastructure in the DRECP.

Mohamed and Verstraeten (2012) presented a technique based on the analysis of multi-temporal Landsat-TM images for studying the dynamics of different dune morphologies. The algorithm (RGB-clustering) was tested at (a) South-Rayan Dune-Field (SRDF), Egypt, (b) Namib Sand Sea (NSS), Namibia. (c) White Sand Dune Field (WSDF), USA, (d) Gran Desierto Sand Sea (GDSS), Mexico, (e) Megabarchanoid ridges, Al Ruba' Al khali (RKH), Saudi Arabia, and (f) Giant linear dunes, Al Ruba' Al Khali (RKH), Saudi Arabia.

We first applied an automated procedure from Mohamed and Verstraeten (2012) in this work for a multi-temporal analysis of sand dune dynamics. The advantage of this methodology is that a variety of dune types, morphologies, and wind regimes can be mapped with high accuracy. This technique showed the good results with dunes developed under uni-directional wind pattern. It has proven easier to detect migration of simple dunes than in compound or complex dunes.

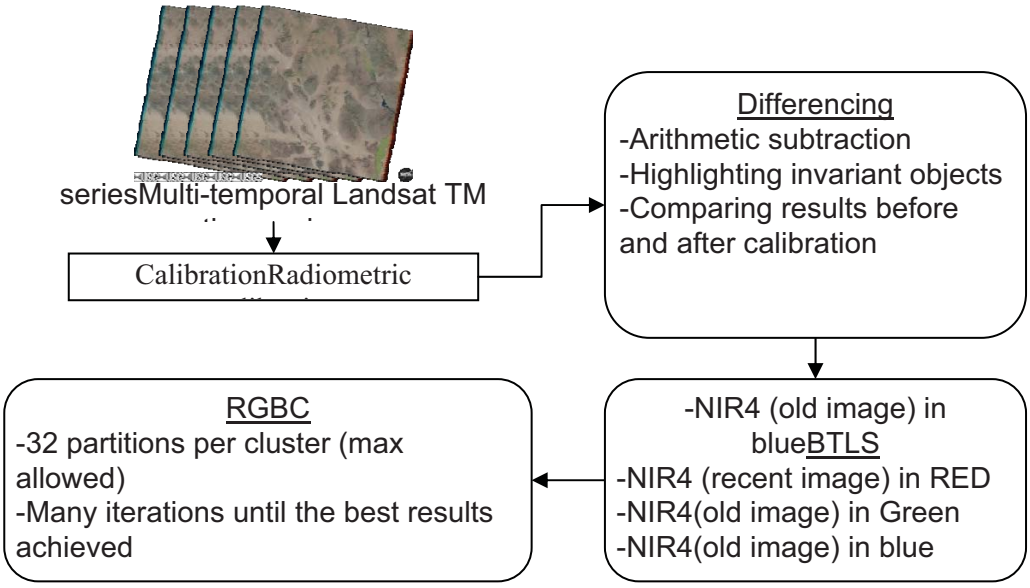

Figure 16.-- Processing scheme for sand dune movement mapping with Landsat TM5 images

- COSI-Corr approach for high resolution aerial imagery

The Co-registration of Optically Satellite Imagery and Correlation (COSI-Corr) (Leprince et al., 2007) is a potential alternative technique for the detection and measurement of sand dune migration. The technique has been developed to detect and measure the subtle crustal deformation in tectonically active areas with a high level of accuracy (Hermas et al., 2012). The COSI-Corr approach has been successfully applied for land surface processes such as glacier (Scherler et al., 2008) and dune movements (Vermeesch & Drake, 2008; Necsoiu et al., 2009; Hermas et al., 2012). In 2012, this technology was also used to map the dynamic of sand dune movement on Mars (*Nature*, http://www.caltech.edu/article/13511, last accessed Feb. 25, 2013).

The COSI-Corr pre-processing steps involved ortho-rectification and co-registration processes of the pre- and post-event images. The correlation process produced a horizontal displacement image composed of three components: east-west, north-south, and signal-to-noise ratio (SNR) (Figure 17). An advantage of the COSI-Corr algorithms, unlike the traditional techniques using field measurements and remote sensing, is that its sub-pixel correlation techniques can provide measurements of sand dune movement over wide spatial coverage at high accuracy (Hermas et al., 2012). The spatial distribution, magnitude, and direction of sand dunes relative to other morphologic units can be well-identified using COSI-Corr algorithms.

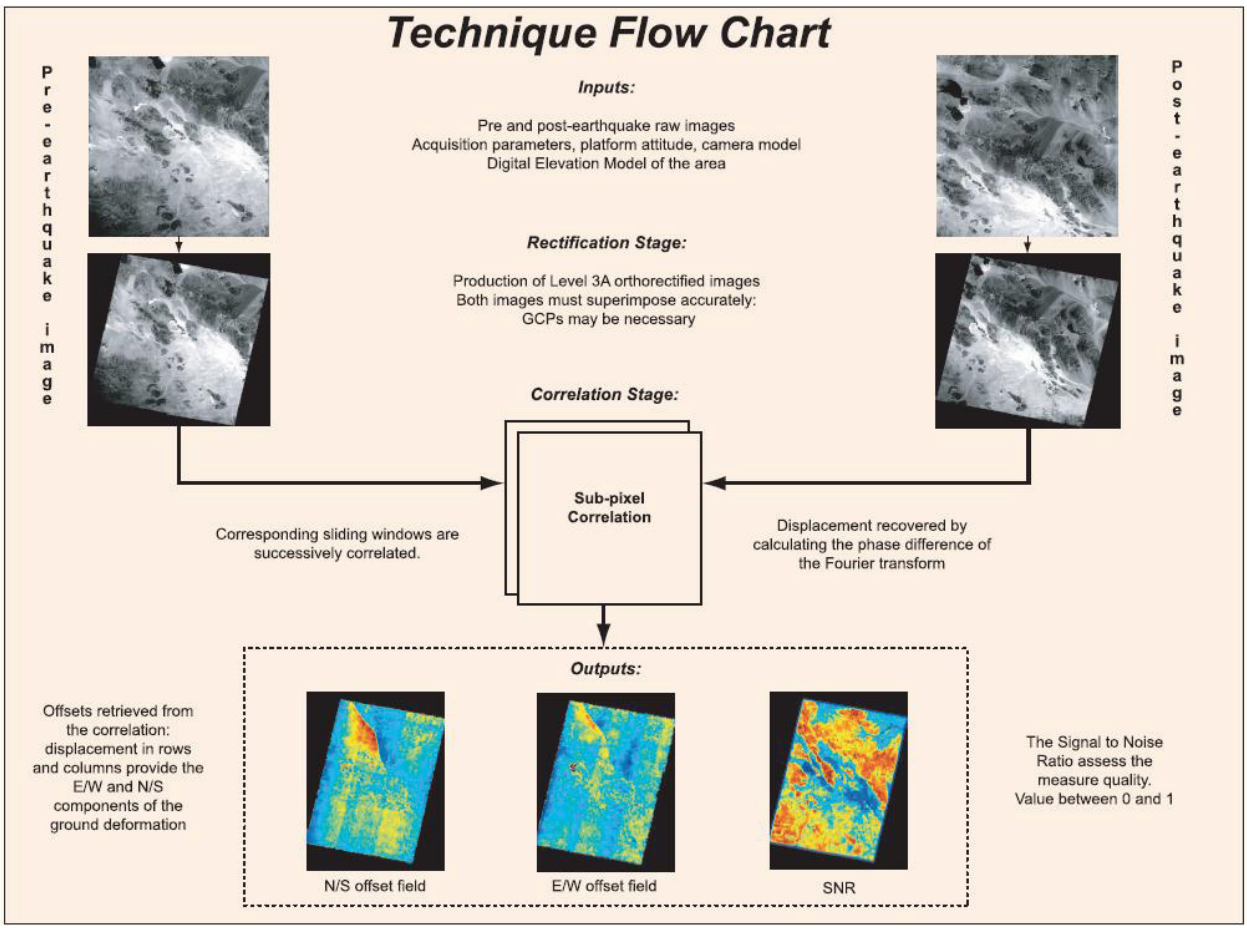

Figure 17.-- Flow chart of COSI-Corr algorithm in producing displacement images from multi-temporal high resolution aerial images (from http://www.tectonics.caltech.edu, last accessed Feb. 25, 2013)

Paleodrainage mapping

Mccauley et al. (1982) first demonstrated the feasibility of subsurface moisture imaging with radar. Low frequency orbital Synthetic Aperture Radar (SAR) has the capability to probe the subsurface down to several meters in arid areas (Paillou et al., 2009). Previous studies have shown that L-band (25 cm or 1.2GHz) SAR is able to penetrate low electrical loss material such as sand (Mccauley et al., 1982; Elachi et al., 1984; Farr et al., 1986). Based on these methodologies, a PALSAR image processing flowchart was generated for this study (Figure 18).

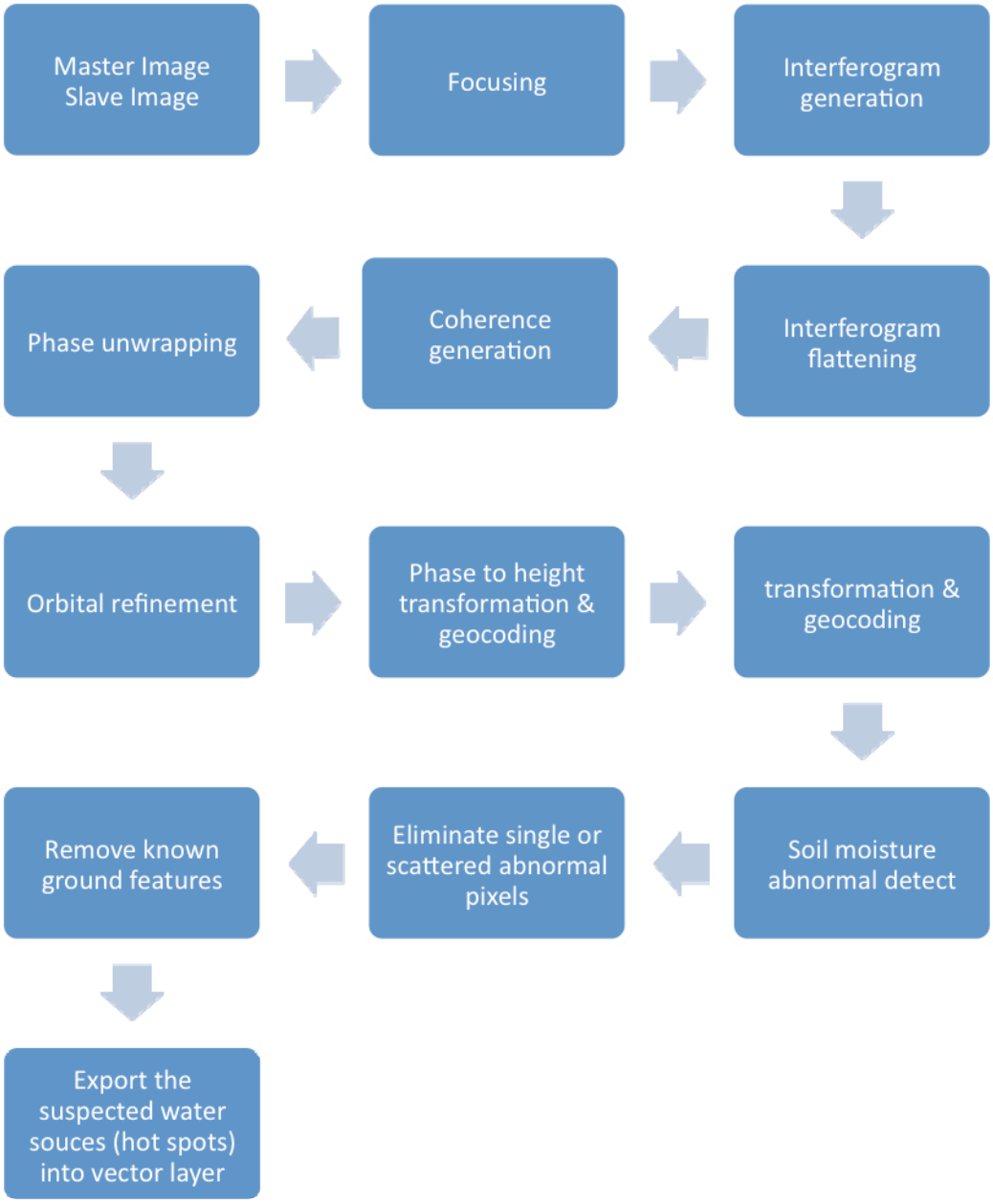

Figure 18. -- Flow chart of subsurface water mapping from ALOS-PALSAR

Desert Map Product Results

Biological Soil Crusts

BSCI maps were created for the entire DRECP study area. **Figure 19** shows the distribution pattern of the BSCI in the Riverside East Solar Energy Zone. Four cover categories were included, based on the BSCI value of the pixels. Two categories of BSC cover were determined form the BSCI, one at >= 33% BSC cover, and the other more uncertain at < 33% BSC cover. In "Background" and "Gravel (desert pavement)" areas, the presence of BSC cover could not be detected.

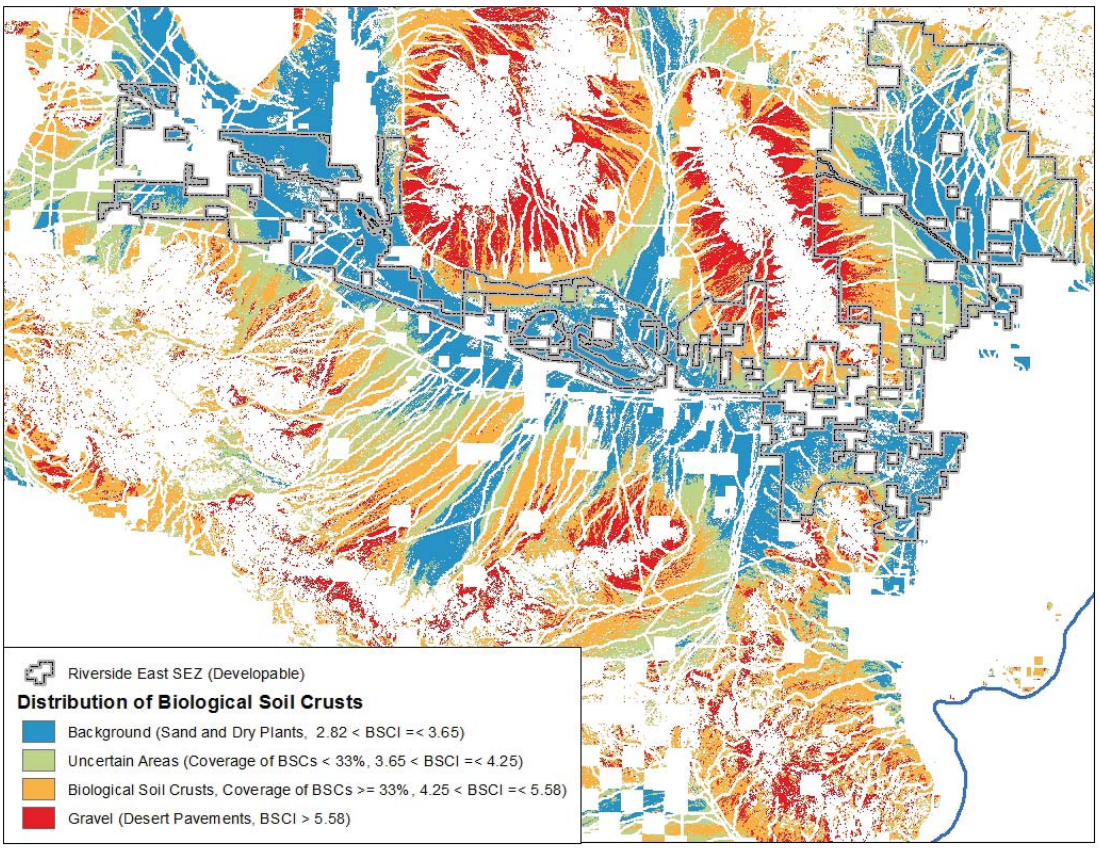

Figure 19.-- The pattern of the BSCI in Riverside East Solar Energy Zone (SEZ)

Datasets listed below were used to mask out non-BSC features from the BSCI product:

- Non-BLM land derived from Land Ownership (updated 01/03/2014)
- Vegetation mask created from NDVI of high-resolution NAIP image.
- Terrain mask generated from the 10-m DEM.
- Buffered (100-m on each side) road and linear water features are from 2013 TIGER linear database

Desert Pavements

A desert pavement is a surface that is covered with closely packed, interlocking angular or rounded rock fragments of pebble and cobble size. Most pavements occur on alluvial fans or alluvial aprons. Desert varnish is visible across the northern Sonoran Desert. The varnish is a hard, dark-brown or black coating, either dull or lustrous (if wind polished), that accumulates on the exposed surfaces of rock fragments and outcrops.

Vesicular horizons are found under the surfaces of many desert pavements (Figure **20**), their distinguishing characteristic being an abundance of unconnected spherical pores (Turk, 2012). Vesicular pores are gas-bubbles that formed within the soil during periods of wetness. Moisture loss in arid soils can be rapid and subject to high evaporation rates. Pulled up through the soil profile via evaporation, these gas-bubbles become essentially "frozen" as the soils dries (Turk, 2012).

Vesicular soil horizons are immediately apparent under the closely packed rock layer. The BSCI was used in this study to detect the distribution of vesicular horizons, defined also as Stage 2 desert pavement. A threshold value (5.4) of BSCI was defined to indicate the probable presence of vesicular horizons. Vesicular horizons detected along the Interstate I-10 highway corridor and across the northern Sonoran Desert were mapped in brown shades below (Figure **21** and Figure 22).

Figure 20. -- Desert pavement with underlying

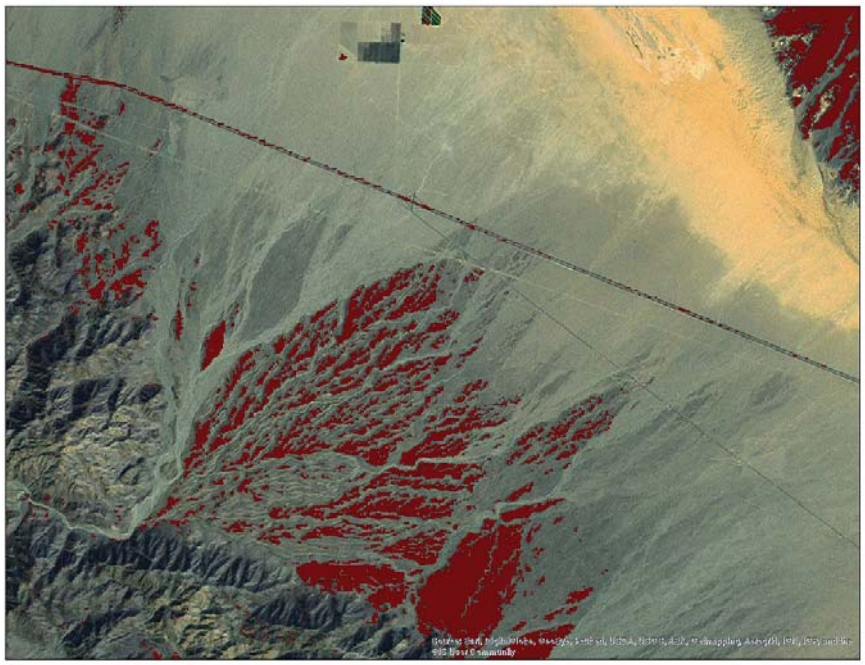

Figure 21.--Vesicular horizons pattern along the I-10 highway corridor

Figure 22. -- Vesicular soil horizons under Stage 2 desert pavements detected in Landsat 5 TM images across the northwestern Sonoran Desert (Colorado Desert)

Band ratios for desert pavement mapping were next calculated from Landsat 5 TM images. Before applying these image analysis steps, pixels with known ground features were masked out (e.g., vegetation, roads, rivers, human structures, and biological soil crusts; Figure 23). Figure 24 shows composite images with red, green, and blue assigned to the three designated band ratios. The RGB clustering approach was further used to divide the areas as Stages 1 and 3 of desert pavement development. Stage 1 included young alluvial fan deposits with active channels and depositional fan surfaces. This stage of development is identified by the presence of distinct bar and swale topography. Stage 3 included old alluvial fan deposits that have been highly dissected, leaving virtually no trace of the original fan surface.

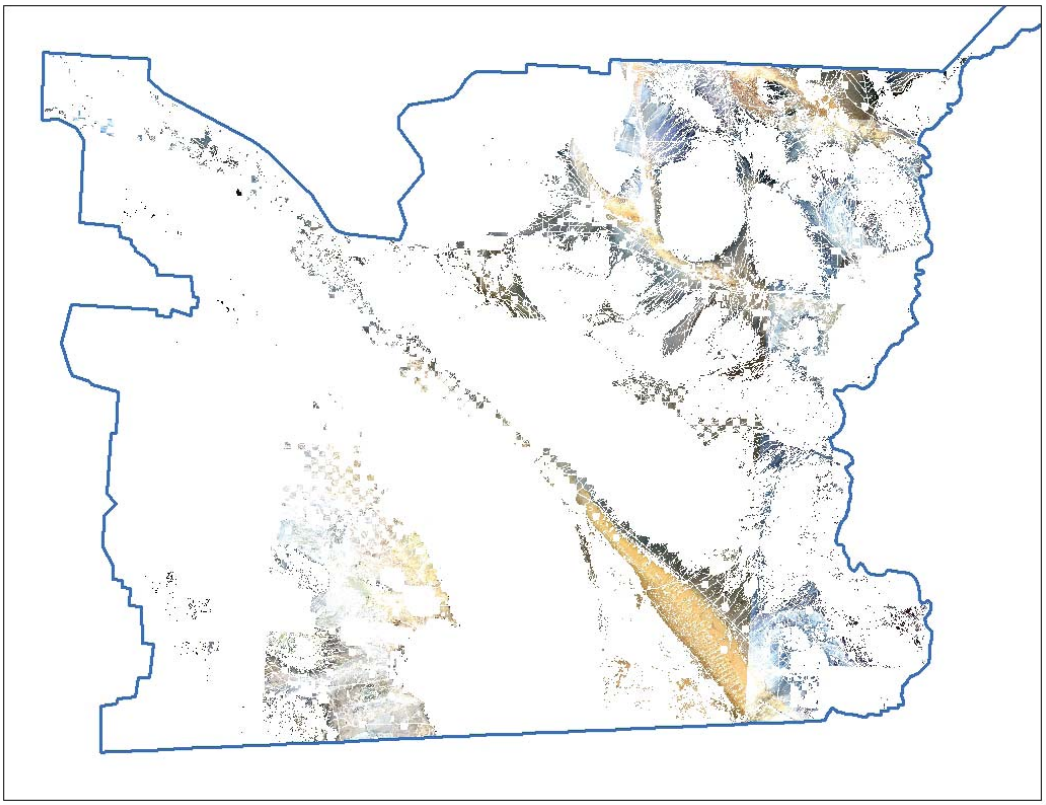

Figure 23.--True color Landsat 5 TM image ready for desert pavement mapping

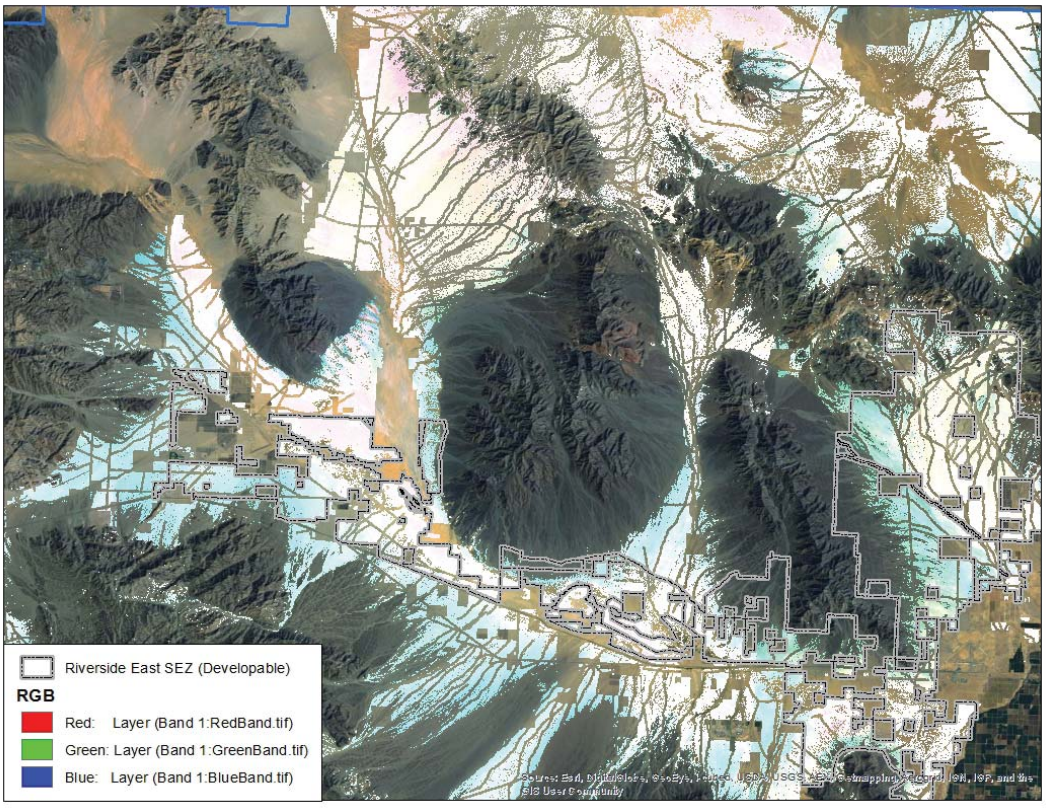

Figure 24.-- Sample of the band-ratio product for desert pavements (Riverside East Solar Energy Zone)

Sand Dune Movements

The near-infrared (NIR) band (0.76-0.90um) of the Landsat 5 TM images has been used to map sand dune migration (see Appendix 1 for field validation report). Two different approaches were applied:

- Approach 1 (BTLS and RGBC)

Step 1: Extract Band 4 from each Landsat scene

Step 2: Co-registration, histogram matching, histogram equalization, and normalization

Step 3: Calculate difference between post- and pre-event of Band 4 layers.

Step 4: Evaluate the effect of histogram matching, histogram equalization, and radiometric normalization by using image differencing. Spectrally stable or invariant objects were identified in the images to check pre-processing effects.

Step 5: Layer stack recent and old Band 4 images into one ENVI DAT file for BTLS analysis.

Step 6: Layer stack images in two specific time periods (post-, pre-event Band4 images) into one DAT file for RGB Classification.

Step 7: Post-process (includes - identify clump, remove sieve (small clumps), and thematic pixel aggregation).

- Approach 2 (COSI-Corr)

Step 1: Prepare the NIR scenes across the investigation time periods.

Step 2: Correlate the pre-event ortho-rectified image (or master image) using the COSI-Corr Fourier correlation engine with the post-event ortho-rectified image.

Step 2: Test correlation parameters with window size and shifting step size in image pixels.

Step 3: Check the layer for signal-to-noise ratio to evaluate the first results.

Step 4: Post-process the horizontal displacement layers and appraise the correlation quality of east-west displacement and north-south displacement.

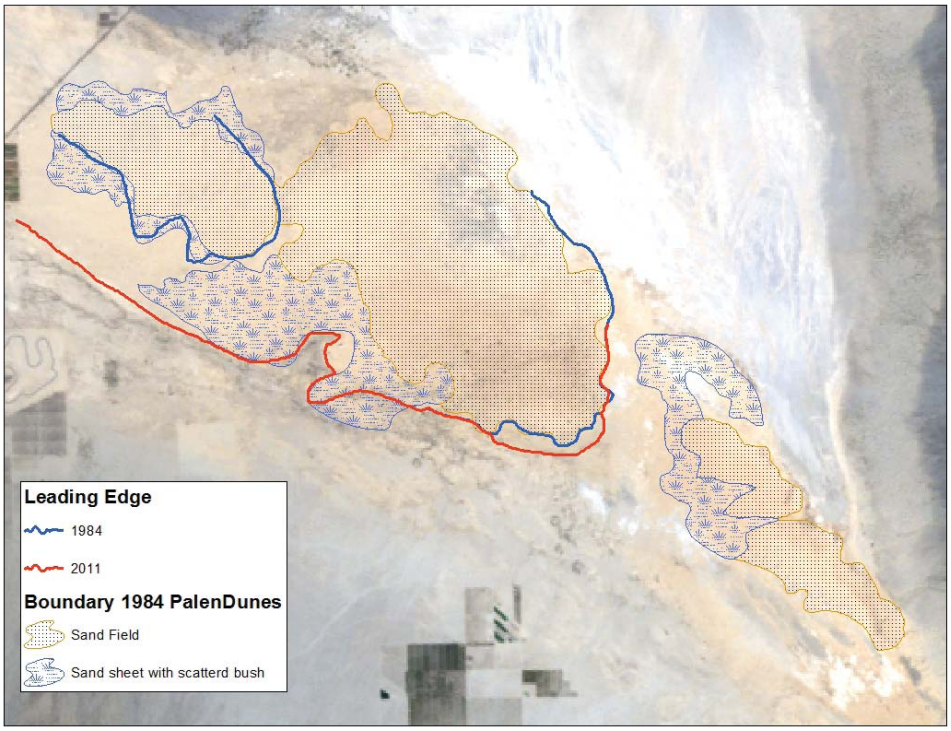

Figure 25.-- Palen Dune migration interpreted from Landsat 5 TM image (baseline boundaries of 1984)

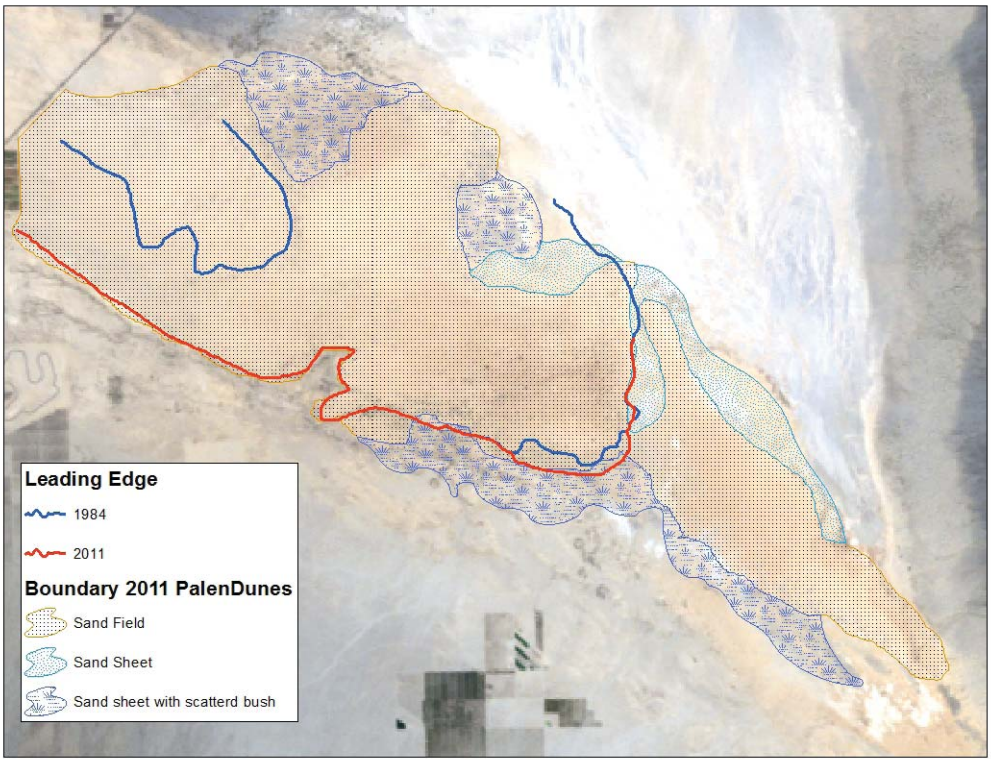

Figure 26.-- Palen Dune migration interpreted from Landsat 5 TM image (baseline boundaries of 2011)

According to the results from BLTS and COSI-Corr approaches, the movement of sand at Palen Dune was delineated as vector layers. Polygon maps were produced that delineated the shift of the leading edges of Palen Dunes between 1984 and 2011 (Figure 25 and Figure 26, respectively). The results from this mapping showed that the rate of dune migration in active regions varied, mostly depending on the original land cover types. Before 1984, sand fields on Palen Dunes were separated by scattered bush and desert grass. Most active dune areas were covered by a thin sand sheet. Only the main dune fields were totally covered by deep sand.

Dune coverage interpreted from 2011 Landsat 5 TM images showed that the two separate sand sheets had become connected and covered most of the areas that had merely scattered vegetation in 1984. We measured dune migration rates as high as 50 meters per year (1373 meters in 27 years, 1984-2011), predominantly in the southern direction, depending on the locality. The overall size of active dune fields increased significantly from 1984-2011. Landsat 5 TM image results showed that the Palen Dunes had grown in areal extent by 47% (from 31 km^2 to 45 km^2) over the past three decades. Active dune areal extent expanded 60% (from 21.3 km^2 to 34.12 km^2) over the same time period. The area covered by scattered bush decreased from 9.2 km^2 to 7.5 km^2.

Suspected water sources under desert surfaces

The results from PALSAR mapping of suspected water source identified numerous "hot spots" with soil moisture abnormalities or signs of a paleodrainage system for subsurface water from radar backscattering. A strong relationship between radar backscattering and soil moisture was demonstrated in Figure 27.

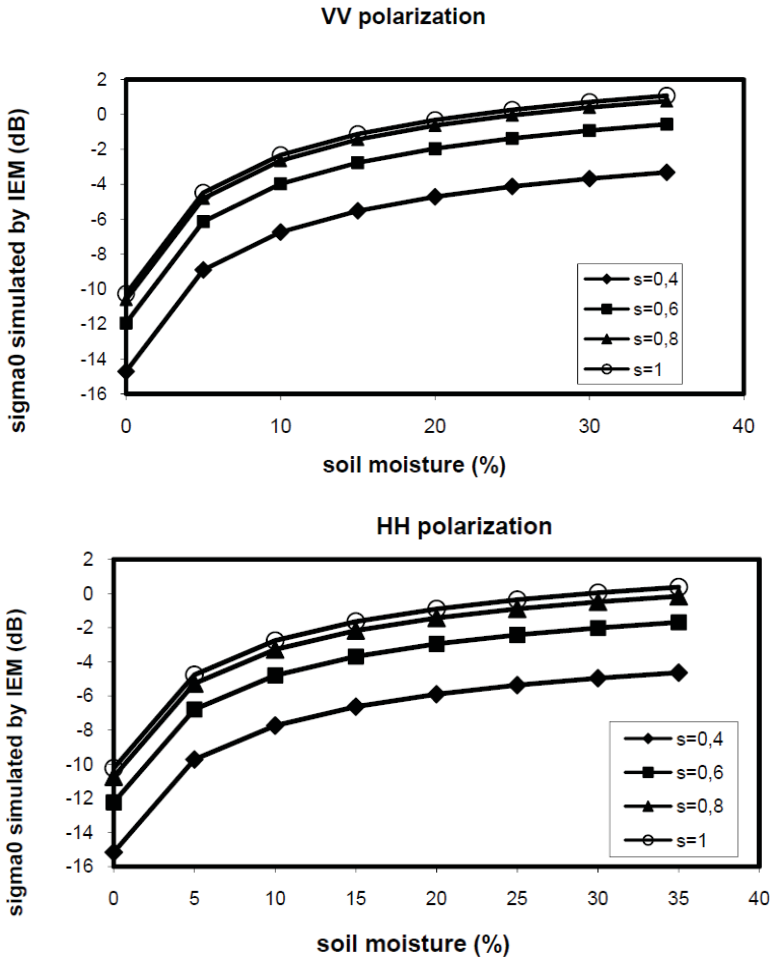

Figure 27.-- Sensitivity of radar backscattering to soil roughness and moisture (after Morvan ea al., 2008)

The following PALSAR analysis steps were followed:

Step 1: A threshold value (greater than -15 dB) of the preprocessed radar backscatter signals was defined to detect soil moisture anomalies across the study area. Pixels of abnormally high soil moisture were exported into a new layer.

Step 2: Single or scattered pixels were removed in the newly created soil moisture anomaly layer. Only clustered pixels were retained for further "hot spot" analysis.

Step 3: Using visual inspection, pixel clusters with known ground features (i.e. high radar backscatter coefficient caused by terrain relief, transmission towers, communication towers, or single buildings) were eliminated from the anomaly layer.

Step 4: All the suspected subsurface water sources were converted into point features. A total of 104 hot spot point locations were identified across the DRECP area (Figure 28).

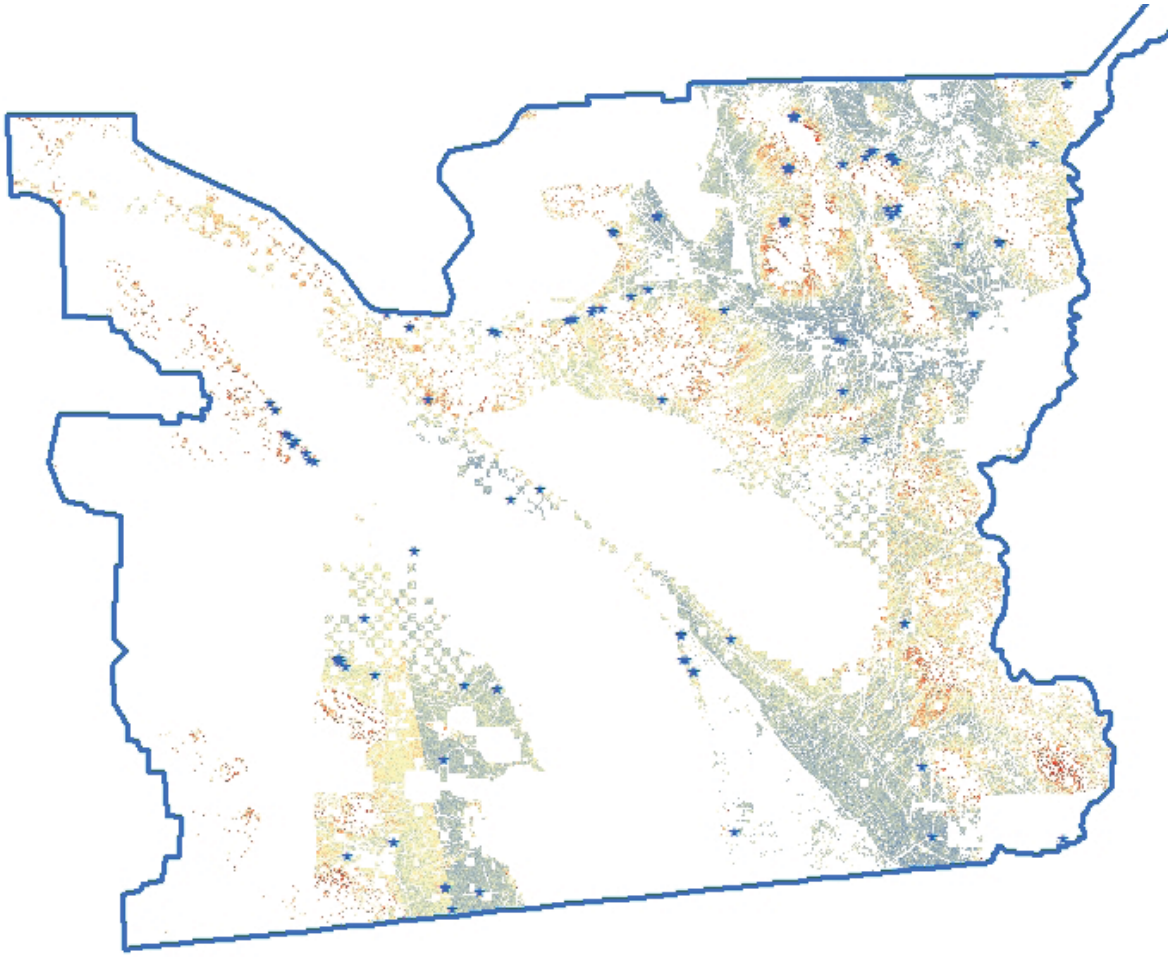

Figure 28.-- Suspected water sources (at blue point locations) from PALSAR image analysis

Conclusions and Next Steps

Methods of image processing were successfully implemented to deliver new maps of BSCs, desert pavements, sand dune movements, and suspected sub-surface water sources across the entire DRECP area. The peer-reviewed methodologies used to generate these new maps have been previously field-validated in the published literature for acceptable accuracy. Nevertheless, next steps for this study may be focused on additional field site visits and more extensive validation of these new map products, mainly in and around areas most likely to be used for renewable energy development.

Close proximity to paved roads and relatively extensive area coverage of the surface features of interest constitute the two main criteria for selecting prime site locations for validation of the new map products. Several candidate locations meeting these criteria could be identified for BSC and desert pavements in the Riverside East SEZ (Figures 29 and 30, respectively). Close proximity to existing or planned renewable energy facilities was a secondary criteria used in selection of candidate locations for field validation.

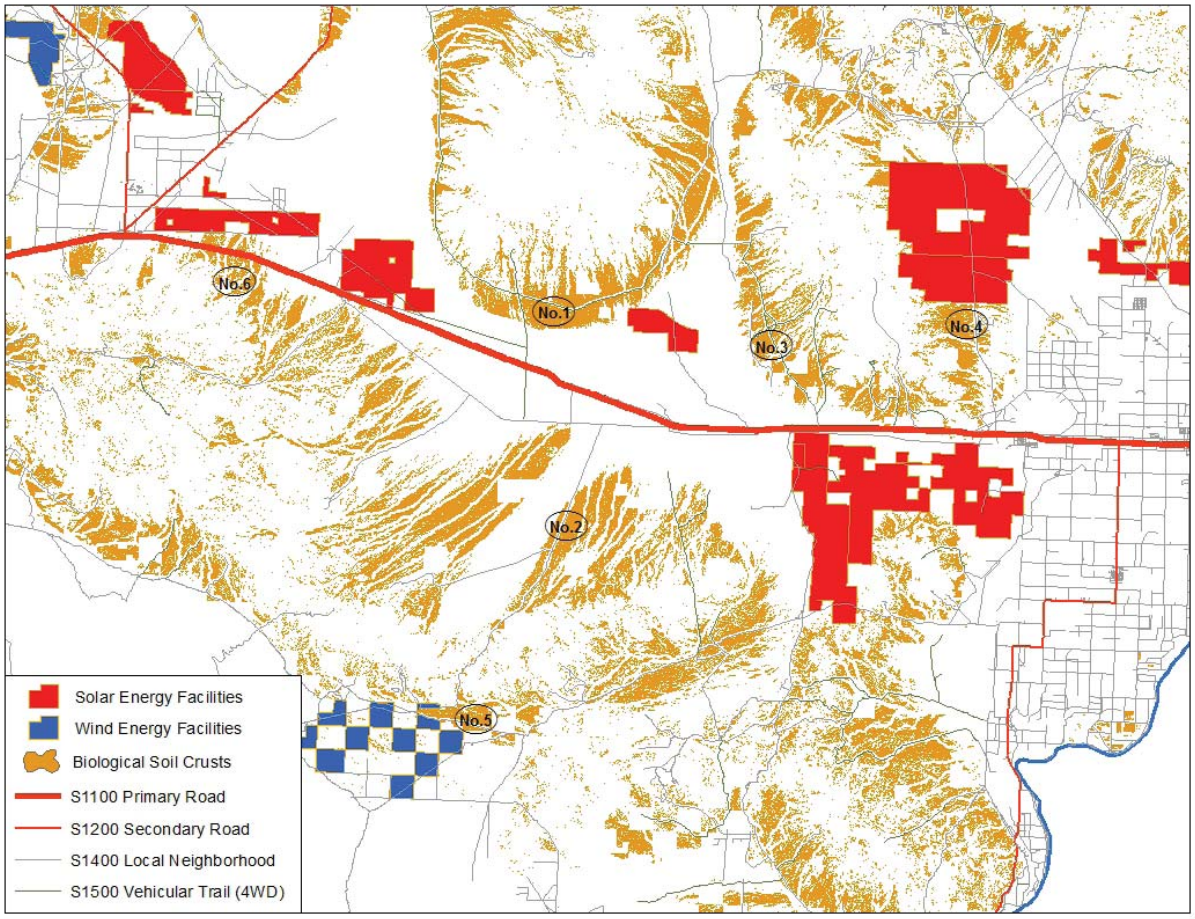

Figure 29. -- Candidate locations for field validation of BSCI mapping for the DRECP

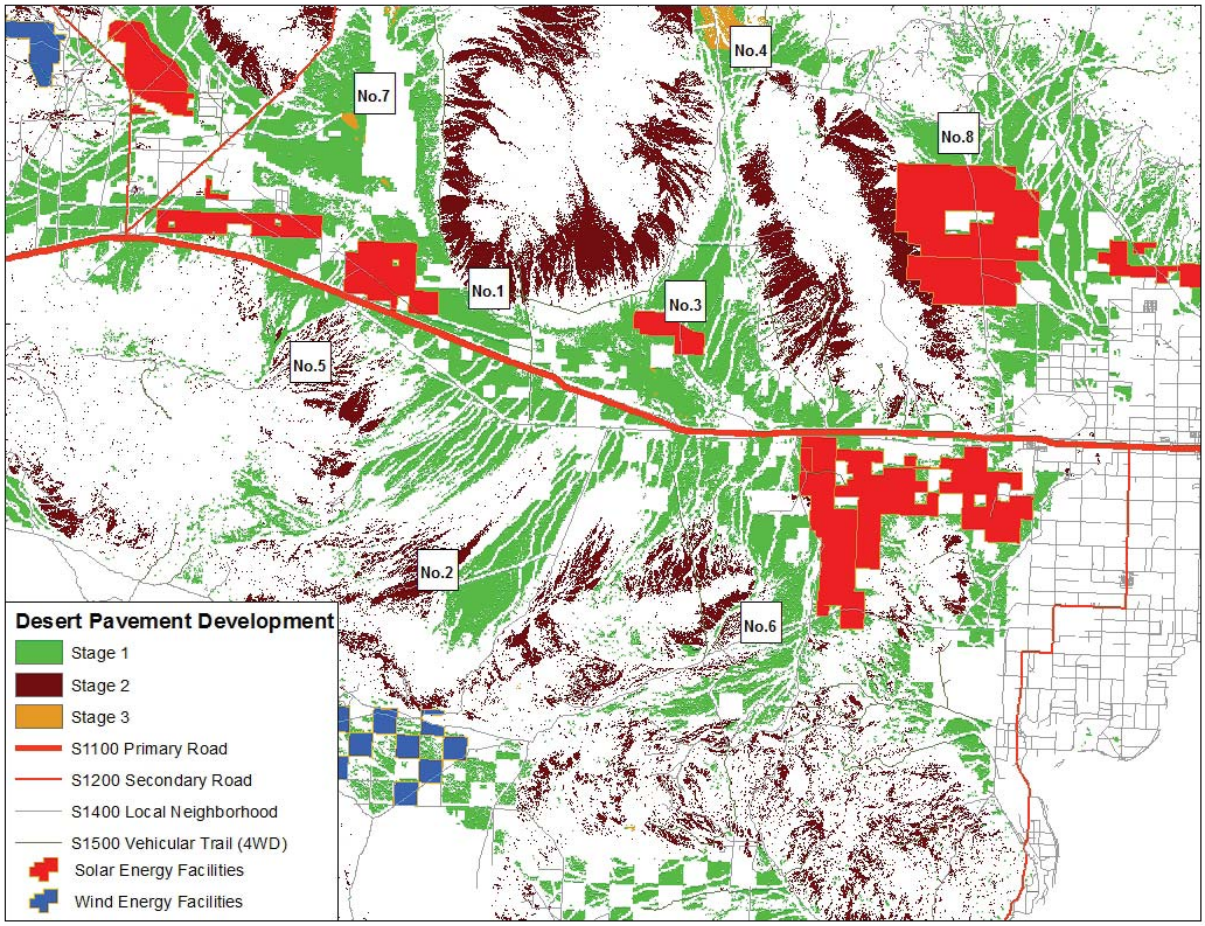

Figure 30. -- Candidate locations for field validation of desert pavement mapping for the DRECP

For the 104 suspected water sources identified from ALOS/PALSAR data, the distances between suspected water source points and a paved road were categorized in Table 5. The distances between suspected water source points and renewable energy facilities (solar and wind) were categorized in Table 6. We found that over 60 suspected water sources identified from ALOS/PALSAR data (see Figure 28) could be within relatively easy access (< 1km buffer zones) from paved roads, making these locations among the highest priority locations for new site visits.

Table 5. -- Distances of the suspected water sources from paved road (US Census Bureau TIGER/Line, 2012)

Buffer zone of paved roads	1 km	2 km	5 km	10 km
Number of water source points	61	94	103	104

Table 6. -- Distances of the suspected water sources from a renewable energy facility (Renewable Energy Project Applications in California Modified: 01/24/2014)

Buffer zone of renewable energy facility	1 km	2 km	5 km	10 km	Greater than 10 km
Number of water source points	8	11	19	26	78

References

Adler-Golden, S.M., Matthew, M.W., Bernstein, L. S., et al. (1999). “Atmospheric Correction for Short-Wave Spectral Imagery Based on MODTRAN4,” in Sum-maries of the Eighth Annual JPL Earth Science Workshop, Vol. I [http://makalu.jpl.nasa.gov], last accessed Jan. 20, 2013.

Ager, C. M., & Milton, N. M. (1987). Spectral reflectance of lichens and their effects on the reflectance of rock substrates. Geophysics, 52, 898-906.

Ben-Dor, E., Chabrillat, S., Demattê, J.A.M., Taylor, G., Hill, J., Whiting, M.L., and Sommer, S. (2009). Using imaging spectroscopy to study soil properties. Remote Sensing of Environment, 113, Suppl. 1, S38-S55.

Beratan, K.K., and Anderson, R. (1998): The use of Landsat Thematic Mapper data for mapping and correlation of Quaternary geomorphic surfaces in the southern Whipple Mountains, California, International Journal of Remote Sensing, 19:12, 2345-2359

Burgheimer, J., Wilske, B., Maseyk, K., Karnieli, A., Zaady, E., Yakir, D., & Kesselmeir, J. (2006). Relationships between Normalized Difference Vegetation Index (NDVI) and carbonfluxes of biological soil crusts assessed by ground measurements. Journal of Arid Environments, 64,651-669

Chen, J., Zhang, M. Y., Wang, L., Shimazaki, H., & Tamura, M. (2005). A new index for mapping lichen-dominated biological soil crusts in desert areas. Remote Sensing of Environment, 96, 165-175.

Clark, R. N., & Roush, T. L. (1984). Reflectance spectroscopy—quantitative-analysis techniques for remote-sensing applications.Journal of Geophysical Research, 89, 6329-6340.

Clark, R. N., Swayze, G. A., & Gallagher, A. (1993). Mapping minerals with imaging spectroscopy (pp. 141−150). Denver, CO: US Geological Survey, Office of Mineral Ressources Bull.

Cooke, R.U., and Warren, A. 1973. Geomorphology in deserts. London: B.T. Batsford Ltd., p. 120.

Elachi, C., Roth, L.E., Schaber, G.G., 1984. Spaceborne radar subsurface imaging in hyperarid regions. IEEE Trans. Geosci. Remote Sens. GE-22, 383-388.

Farr, T.G., Elachi, C., Hartl, P., Chowdhury, K., 1986. Microwave penetration and attenuation in desert soil: a field experiment with the shuttle imaging radar. IEEE Trans. Geosci. Remote Sens. GE-24 (4), 590–594

Graetz, R. D., & Gentle, M. R. (1982). The relationship between reflectance in the Landsat wavebands and the composition of an Australian semi-arid shrub rangeland. Photogrammetric Engineering and Remote Sensing, 48, 1721-1730

Hermas, E., Leprince, S., and El-Magd, I.A. (2012). Retrieving sand dune movements using sub-pixel correlation of multi-temporal optical remote sensing imagery, northwest Sinai Peninsula, Egypt. Remote Sensing of Environment, 121:51-60

Jacobberger, P. A. (1989). Reflectance characteristics and surface processes in stabilized dune environments. Remote Sensing of Environment, 28, 287-295

Karnieli, A., Kokaly, R. F., West, N. E., & Clark, R. N. (2001). Remote sensing of Biological Soil Crusts. In J., & O. L. (Eds.),Ecological studies 150: Biological Soil Crusts: Structure, function, and management(pp. 431−455).Berlin: Springer.

Karnieli, A., & Sarafis, V. (1996). Reflectance spectrophotometry of cyanobacteria within soil crusts—A diagnostic tool. International Journal of Remote Sensing,17,1609-1614

Karnieli, A., Kidron, G. J., Glaesser, C., & Ben-Dor, E. (1999). Spectral characteristics of cyanobacteria soil crust in semiarid environments. Remote Sensing of Environment, 69, 67-75.

Karnieli, A., Shachak, M., Tsoar, H., Zaady, E., Kaufman, Y., Danin, A., & Porter, W. (1996). The effect of microphytes on the spectral reflectance of vegetation in semiarid regions. Remote Sensing of Environment, 57, 88-96.

Karnieli, A., & Tsoar, H. (1995). Satellite spectral reflectance of biogenic crust developed on desert dune sand along the Israel–Egypt border. International Journal of Remote Sensing, 16, 369-374.

Kocurek, G., Ewing, R.C., 2005. Aeolian dune field self-organiza-tion - implications for the formation of simple versus complex dune-field patterns. Geomorphology 72, 94-105.

Kokaly, R. F., Clark, R. N., & Swayze, G. A. (1994). Vegetation and cryptobiotic soils mapping in arid regions.Spectral analysis workshop: The use of vegetation as an indicator of environmental contamination. Desert Research Institute, Reno, Nevada, November 9–10, 1994 http://speclab.cr.usgs.gov/PAPERS.arches.crypto.94/arches.crypto.dri.html

Le Morvan, A.; Zribi, M.; Baghdadi, N.; Chanzy, A. Soil Moisture Profile Effect on Radar Signal Measurement. Sensors 2008, 8, 256-270.

Leprince, S., Barbot, S., Ayoub, F., and Avouac, J. (2007). Automatic and precise orthorec-tification, coregistration, and subpixel correlation of satellite images, application to ground deformation measurements. IEEE Transactions on Geoscience and Remote Sensing, 45(6), 1529-1558.

Livingstone, I., Wiggs, G.F.S., & Weaver, C.M. (2007). Geomorphology of desert sand dunes: A review of recent progress. Earth-Science Reviews, 80, 239-257.

Mccauley, J.F., Schaber, G.G., Breed, C.S., Grolier, M.J., Haynes, C.V., Issawi, B., Elachi, C., Blom, R. (1982). Subsurface valleys and geoarchaeology of the eastern Sahara revealed by Shuttle radar, Science, 218: 1004-1020

Mohamed, I., and Verstraeten, G. (2012). Analyzing dune dynamics at the dune-field scale based on multi-temporal analysis of Landsat-TM images. Remote Sensing of Environment, 119: 105-117.http://dx.doi.org/10.1016/j.rse.2011.12.010

Necsoiu, M., Leprince, S., Hooper, D. M., Dinwiddie, C. L., McGinnis, R. N., & Walter, G. R. (2009). Monitoring migration rates of an active subarctic dune field using optical imagery. Remote Sensing of Environment, 113, 2441-2447

Paillou, P., Schuster, M., Tooth, S., Farr, T., Rosenqvist, A., Lopez, S., Malezieux, J.M. (2009). Mapping of a major paleodrainage system in eastern Libya using orbital imaging radar: The Kufrah River. Earth and Planetary Science Letters, 277(3-4): 327-333

Potter, R.M., and Rossman, G.R. (1979). The manganese and iron-oxide mineralogy of desert varnish. Chemical Geology, 25: 79-94.

Redsteer, M.H, Bogle, R.C., and Vogel, J.M. (2011) Monitoring and analysis of sand dune movement and growth on the Navajo Nation, southwestern United States: U.S. Geological Survey Fact Sheet 2011–3085, 2 p., available at http://pubs.usgs.gov/fs/2011/3085/.

Song, C., Woodcock, C. E., Seto, K. C., Lenney,M. P. and Macomber, S. A. (2001). Classification and Change Detection Using Landsat TM Data: When and How to Correct Atmospheric Effects? Remote Sensing Environment, 75, 230-244.

Scherler, D., Leprince, S., and Strecker, M. R. (2008). Glacier-surface velocities in alpine terrain from optical satellite imagery—Accuracy improvement and quality assessment. Remote Sensing of Environment, 112, 3806-3819.

Turk, J. K. (2012). Vesicular Horizon Distribution, Properties, and Pedogenic Processes in Deserts of the Western United States. Dissertation submitted to the University of California Riverside, Soil and Water Sciences. 211 pp.

Vermeesch, P., & Drake, N. (2008). Remotely sensed dune celerity and sandflux measurements of the world's fastest barchans (Bodele, Chad).Geophysical Research Letters,35, L24404 6 PP. (Necsoiu et al., 2009; Vermeesch & Drake, 2008).

Werner, B.T. (1995). Eolian dunes: computer simulations and attractor interpretation. Geology 23, 1107-1110.

Weber, B., Olehowski, C., Knerr, T., Hill, J., Deutchewitz, K., Wessels, D.C.J., Eitel, B., and Büdel, B. (2008). A new approach for mapping of Biological Soil Crusts in semidesert areas with hyperspectral imagery. Remote Sensing of Environment 112: 2187-2201.

Appendix 1. Validation of Landsat Image Analysis for Mapping Sand Dune Movements

Background

Landsat images have been used to study the mineralogy of sand dunes, dune morphological parameters, and dune migration rates in deserts around the world. The method of RGB-clustering with Landsat Thematic Mapper (TM) imagery (as reviewed by Mohamed and Verstraeten, 2012) is a technique to map the movement of sand dunes in arid regions from readily available satellite imagery. In order to apply this Landsat RGB-clustering methodology with confidence over the southern California desert region, we have carried out validation using measurements and analysis results from USGS scientists who are monitoring sand dune movement on Navajo Nation lands of Arizona (Figure 1; Redsteer et al., 2011). This USGS research revealed the dynamic migration rate of the Grand Falls dune field from 1953 to 2010. Global positioning system (GPS) and ground-based LiDAR (light detection and ranging) measurements were used to monitor the migration rate of the sand dunes in Arizona.

Figure 1.-- Location of Grand Falls dune movement study site (from Redsteer et al., 2011)

Multi-temporal Landsat-TM imagery

Landsat TM5 scenes were collected from the USGS EarthExplorer (http://earthexplorer.usgs.gov/) and processed with Standard Terrain Correction (Level 1T). These Landsat images (Table 1) were selected to correspond (as closely as possible) to the measurement periods of Grand Falls dune field studies by Redsteer et al. (2011).

Table 1. -- Landsat TM5 images used for the mapping of sand dune migration

Acquisition Date	Image ID	Sun Azimuth	Sun Elevation
07/4/1984	LT50370351984186PAC00	108.82	60.96
08/27/1992	LT50370351992240XXX02	125.63	51.71
06/22/1997	LT50370351997173XXX02	108.75	62.04
08/31/2005	LT50370352005243PAC01	135.78	54.75
08/13/2010	LT50370352010225PAC01	128.08	59.26

Description of the RGB-clustering Methodology

Criteria used in Landsat image selection (Figure 2 and Table 1)

- Best available radiometric, geometric, and atmospheric quality;
- Bi-temporal images were acquired at the same time of the year;
- Sun direction of a TM scene was perpendicular to the dune crest or at the stoss side, and the sun elevation angle was greater than 30 degrees

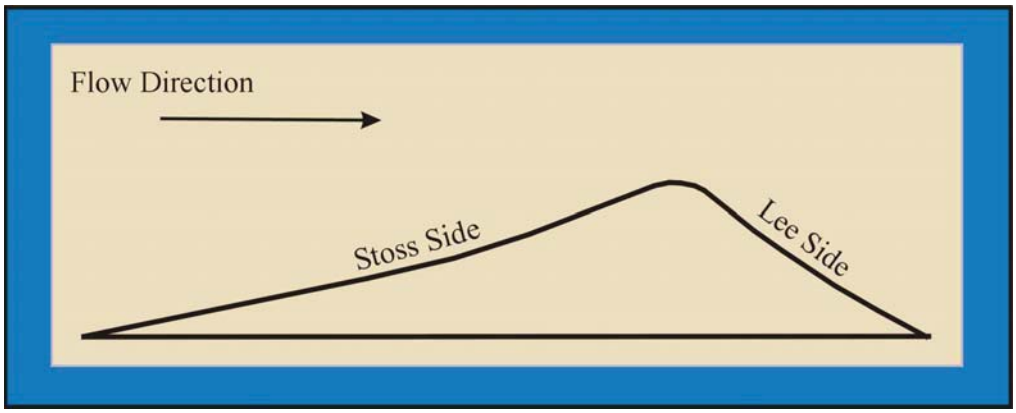

Figure 2.-- Diagram of stoss and lee sides of a sand dune (Source: University of Wisconsin-Milwaukee)

Bi-temporal layerstack (BTLS)

The approach of a Bi-Temporal Layer Stack (BTLS) has its origin from Write Function Memory Insertion (WFMI) methods, which was first presented by Jensen (1996). WFMI is a visual change-detection technique, where single bands from multi-temporal satellite images are displayed in specific colors (typically red, green and blue). Mohamed and Verstraeten (2012) applied WFMI to multi-temporal Landsat images to detect the dynamics of sand dune movement (see Figure 3).

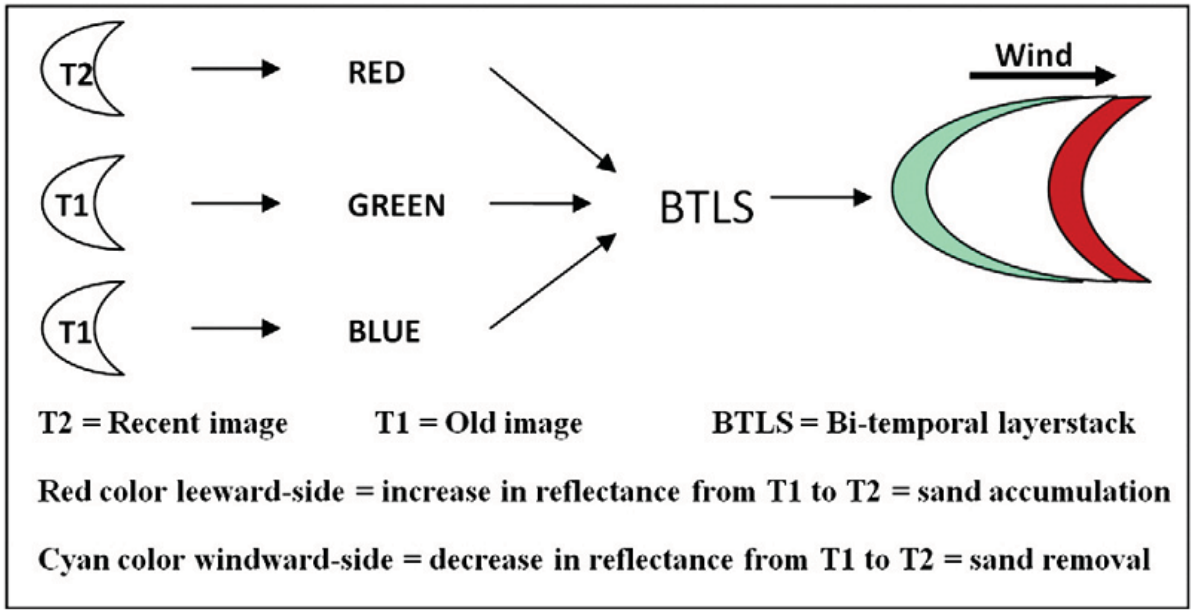

Figure 3.-- Illustration of the basic principle of bi-temporal layer stacking (BTLS) for detecting dune migration (after Mohamed and Verstraeten, 2012)

RGB-clustering for multi-temporal Landsat TM images

RGB-Clustering methodology was used to compress three bands of data into one and to perform simple unsupervised classification. The RGB clustering method is more specialized than the Self-Organizing Data Analysis Technique (ISODATA) method, since it applies to three-band, 8-bit data (ERDAS, 2011; see Figures 4 and 5).

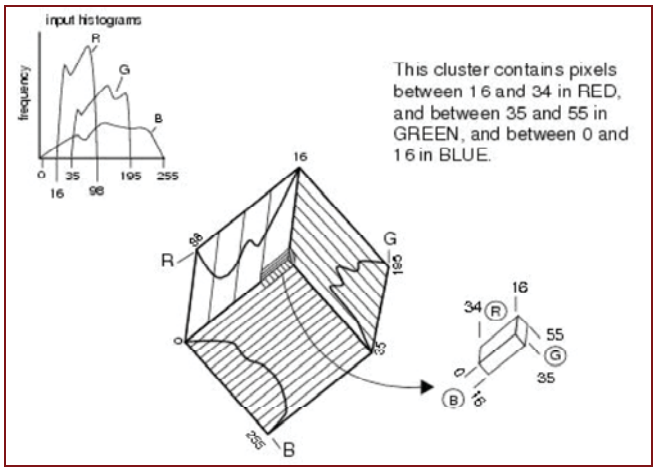

Figure 4.--Diagram of RGB clustering methodology

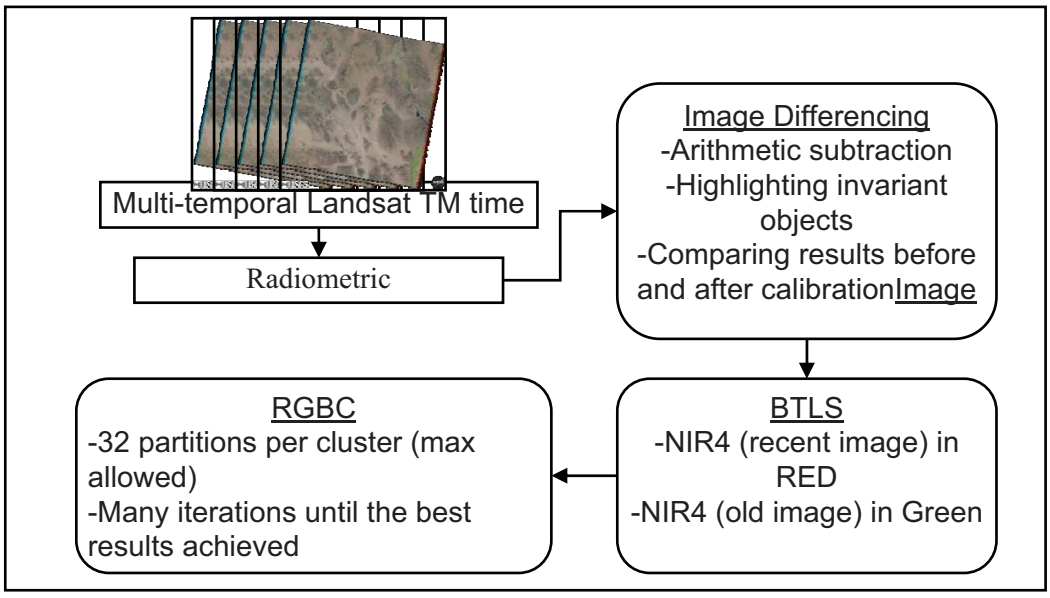

Figure 5.--Processing scheme for sand dune mapping with Landsat TM5 images

Results

Using the BTLS approach with Landsat TM images, we estimated the migration rate and direction of the Grand Falls dune field from 1984 to 2010. The post-event NIR band was displayed in the red color to express the increase in reflectance (Figure 6). The pre-event NIR band was displayed in both the green and blue channels to represent the stoss side of the sand dune in a cyan color (i.e., a decrease in reflectance).

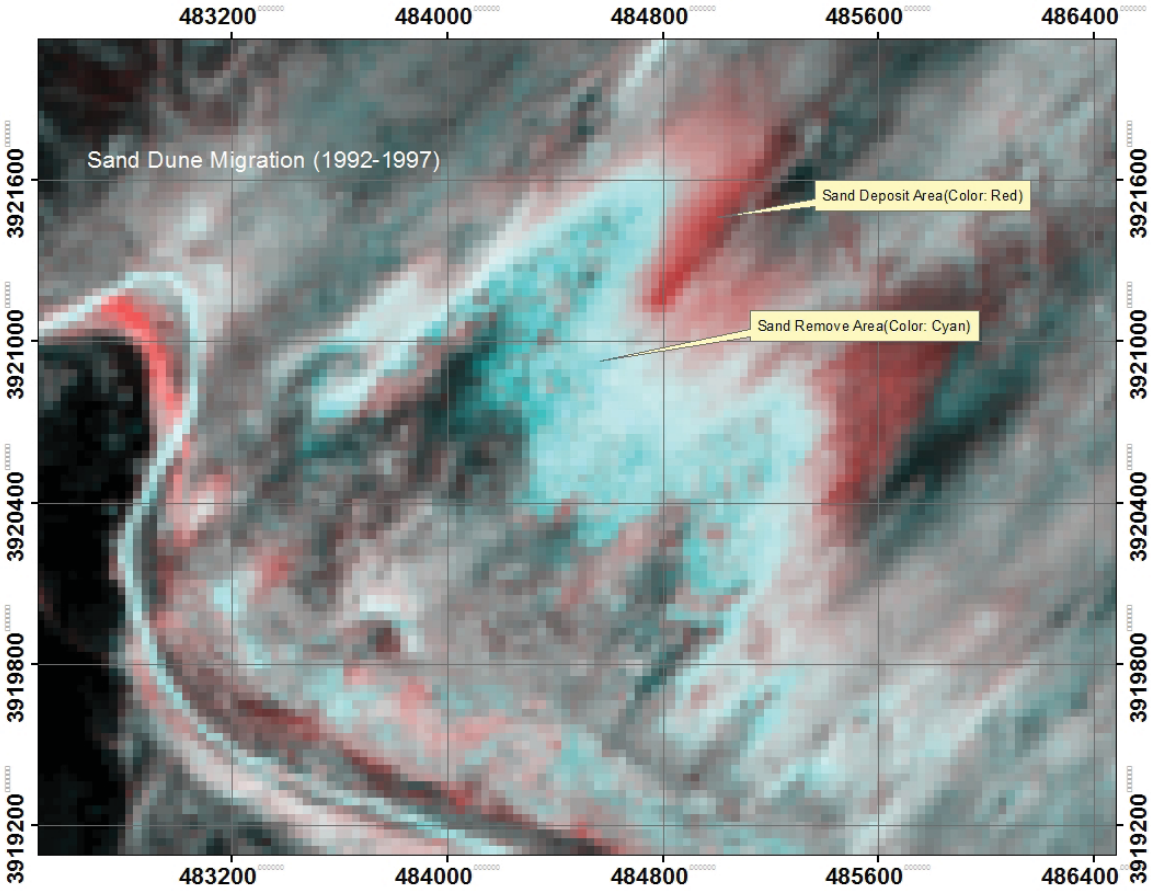

Figure 6.-- BTLS map results of Grand Falls dune field on the Navajo Nation

By adjusting the bin numbers of RGB classes during clustering, the pixels representing sand movement were matched to Landsat BTLS maps. The new raster layer from RGB-clustering was used to estimate the migration rates of dunes in the Grand Falls dune field from 1992 through 2010. We noted that Landsat pixels located on the southwest corner of the dune field were misclassified as sand. This area is apparently covered by riparian or wetland vegetation. The RGB-clustering approach cannot correctly discriminate this land cover type from sand erosion and deposition areas. We would recommend that a vegetation/barren mask layer from the National Land Cover Dataset (NLDC) be applied before the RGB-clustering method is used on a larger desert region for dune migration mapping.

In order to evaluate the results from BTLS and RGB-clustering, we created more than 1600 dot pairs of vertices along the four leading dune edge lines (1992, 1997, 2005, and 2010) for comparison to measured migration distances. The leading edges from USGS measurements were considered the baselines in this dot pair Euclidian distance comparison with Landsat-estimated leading edges (Figure 7).

For the leading-edge polyline comparisons shown in Figure 7, the predominant SW-to-NE direction of sand dune movements was the same between the baseline USGS measurements and Landsat image results. The smallest average difference between dot pairs was found for the 2005 leading edge at less than 1-meter difference (Table 2). Among the other comparison years, the largest difference between dot pairs occurred in 2010 at an average of 50 m, which is still less than a 2-pixel width error in the 30-m resolution Landsat TM images. The leading edge for 1992 detected from Landsat imagery was the only edge lagging behind the leading edge delineated by USGS measurements, by an average of 46 m.

Table 2.-- Leading edge differences between dot pairs of Landsat RGB-clustering and USGS measurements of sand dune migration

	Dot Pairs	Max (m)	Min (m)	Average (m)	StdDev
2010	517	151.80	-64.85	50.15	48.58
2005	399	58.69	-174.64	0.08	34.68
1997	388	131.70	-64.85	39.73	53.20
1992	390	59.08	-294.76	-45.62	82.40

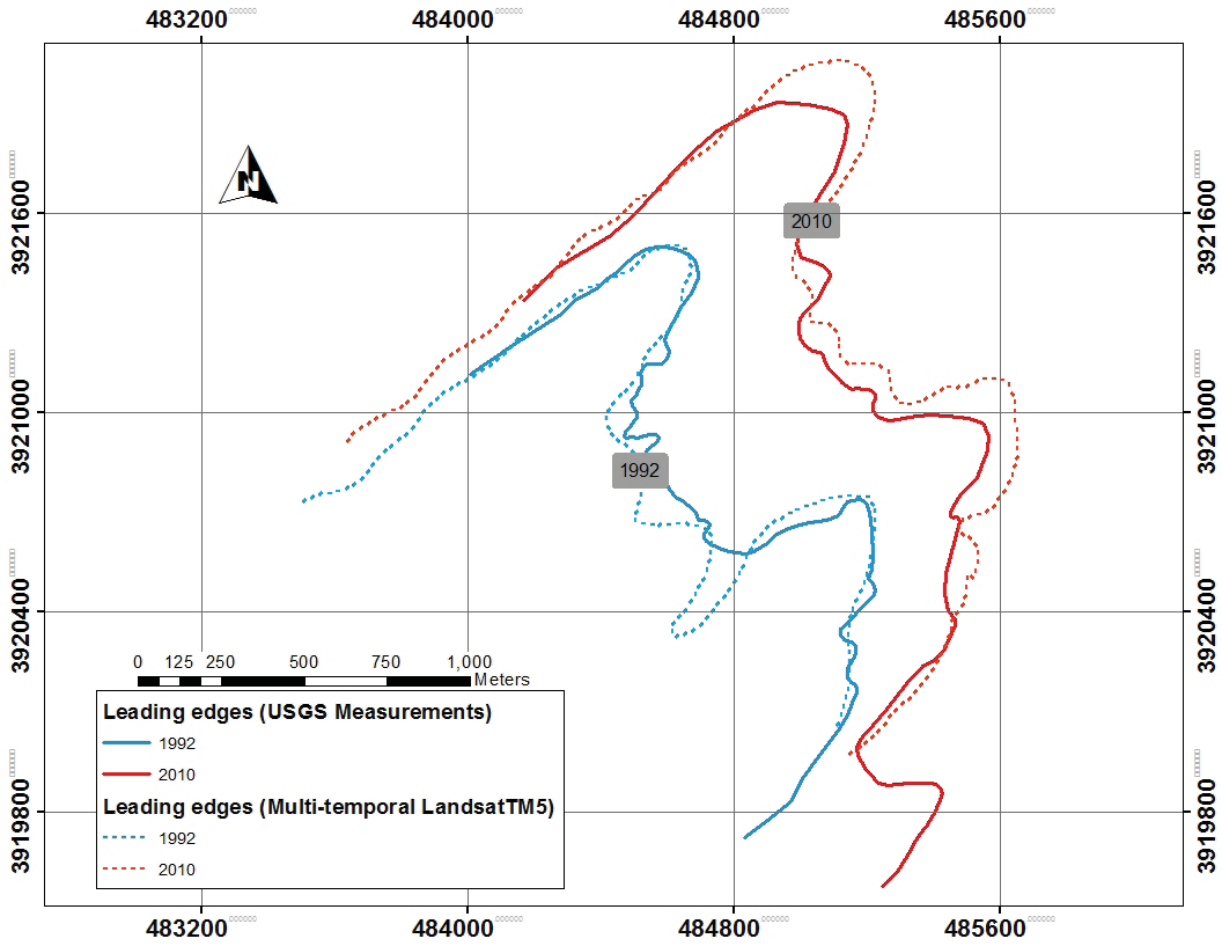

Figure 7.-- Difference of sand dune migration-rate between RGB-clustering algorithm and USGS measurements of dune leading edges

Comparisons of Landsat-estimated maximum dune migration rates in the Grand Falls dune field with measured rates from USGS showed that USGS-measured maximum migration rates were 20-60% lower than the Landsat-estimated distances during all periods (except the 1997-2005 time period; Table 3). The closest match of maximum annual dune migration rates between the two methods were found for the 1997-2005 time period and over the entire 1992-2010 period, at less than 15 m difference, which is less than one-half the width of a Landsat TM pixel. The overall difference between the Landsat image and USGS measurement results in maximum dune migration rates between 1992 and 2010 was about 145 meters, which is equivalent to five Landsat pixels, compared to an equivalent of nearly 25 pixel distances detected in this overall (18-year) maximum migration distance.

Table 3.-- Comparison of maximum migration rates in the Grand Falls dune field

Time period	Distance between two leading edges (meters)		Annual migration-rate (m/yr)	
	USGS	Landsat	USGS	Landsat
1992-1997	156	260	31.2	52.0
1997-2005	355	249	44.4	31.1
2005-2010	105	253	21.0	50.6
1992-2010 total	616	762	34.2	42.3

There are several possible explanations for the modest differences detected between Landsat image results and USGS measurements of sand due migration in the Grand Falls dune field (Figure 7). First, the exact dates of the leading edges delineated by USGS researchers were not known to us. One winter/spring windy season may cause the dune fields to migrate more than 30 m, and since most of the Landsat images used in this study were captured in the cloud-free summer period, there may have been mismatches in timing of the satellite images and USGS measurements. Next, since the spatial resolution of Landsat images is coarser than the 1-m resolution measurements surveyed by USGS investigators, an average error level of just under two 30-m Landsat pixels would not be unexpected. Finally, the 30-50 m level of spatial accuracy in dune migration rates from 1992 to 2010 may be accounted for by the unavoidable shading effects of the leading edges of sand dunes captured by Landsat images.

Conclusions

Landsat image analysis of the Grand Falls dune field resulted in accurate mapping of sand dune migration rates, compared to measurements surveyed by USGS investigators from 1992 to 2010. The predominant direction of sand dune movements was correctly mapped at this site from the Landsat satellite imagery, as well as the migration distances of the leading edges of sand dunes over the entire 1992-2010 monitoring period. Application of dune migration rate results from Landsat images collected for this validation study can be extended over a large portion of the Navajo Nation in Arizona and eventually over much of sandy desert areas of the southwestern United States.

Acknowledgements

The authors thank USGS scientists Margaret Hiza Redsteer, John Vogel, and Rian Bogle for sharing sand dune migration data sets used for this evaluation study.

References

Mohamed, I., and Verstraeten, G. (2012). Analyzing dune dynamics at the dune-field scale based on multi-temporal analysis of Landsat-TM images. *Remote Sensing of Environment*, 119: 105-117.http://dx.doi.org/10.1016/j.rse.2011.12.010.

Redsteer, M.H, Bogle, R.C., and Vogel, J.M. (2011) Monitoring and analysis of sand dune movement and growth on the Navajo Nation, southwestern United States: U.S.

Geological Survey Fact Sheet 2011–3085, 2 p., available at http://pubs.usgs.gov/fs/2011/3085/.

Levin, N., Ben-Dor, E., & Karnieli, A. (2004). Topographic information of sand dunes as extracted from shading effects using Landsat images. *Remote Sensing of Environment*, 90, 190-209.

Jensen, J. R. (1996). Introductory digital image processing: A remote sensing perspective. Upper Saddle River, New Jersey: Prentice Hall.

ERDAS (2011). ERDAS Imagine 2011, Field Guide. 2011.Atlanta: ERDAS Inc. Geosystem. http://www.erdas.com